Adjoint measurement and calibration of Manning roughness in E3SM's river dynamical core

Mark F. Adams[1] mfadams@lbl.gov
Gautam Bisht[2] gautam.bisht@pnnl.gov
Donghui Xu[2] donghui.xu@pnnl.gov
Jeffrey Johnson[3] jeff@cohere-llc.com
Jed Brown[4] jed@jedbrown.org
Matthew Knepley[5] knepley@gmail.com

[1]Applied Mathematics & Computational Research Division, Lawrence Berkeley National Laboratory, Berkeley, CA, USA
[2]Atmospheric, Climate, & Earth Sciences Division, Pacific Northwest National Laboratory, Richland, WA, USA
[3]Cohere Consulting, LLC, Seattle, WA, USA
[4]Department of Computer Science, University of Colorado Boulder, Boulder, CO, USA
[5]Computer Science and Engineering, University at Buffalo, Buffalo, NY, USA

Corresponding author: Mark F. Adams, mfadams@lbl.gov

Peer review status:

This is a non-peer-reviewed preprint submitted to EarthArXiv.

Adjoint measurement and calibration of Manning roughness in E3SM's river dynamical core

Mark F. Adams[1], Gautam Bisht[2], Donghui Xu[2], Jeffrey Johnson[3], Jed Brown[4], Matthew Knepley[5]

[1]Applied Mathematics & Computational Research Division, Lawrence Berkeley National Laboratory, Berkeley, CA, USA

[2]Atmospheric, Climate, & Earth Sciences Division, Pacific Northwest National Laboratory, Richland, WA, USA

[3]Cohere Consulting, LLC, Seattle, WA, USA

[4]Department of Computer Science, University of Colorado Boulder, Boulder, CO, USA

[5]Computer Science and Engineering, University at Buffalo, Buffalo, NY, USA

Abstract

This paper presents a transient discrete adjoint of RDycore, the river dynamical core of the Energy Exascale Earth System Model (E3SM), and uses it to measure how much of a flood model's error its roughness parameter is able to remove. We differentiate the production solver in place rather than rewrite it in a differentiable-programming framework: one exact, assembled Jacobian of the shallow-water right-hand side serves the implicit time integrator, the adjoint, and the calibration. An objective and its gradient cost about two forward solves regardless of the number of parameters, every derivative passes a finite-difference gate on the full nonlinear solve, and the whole computation runs on GPUs, forward model and derivatives alike, where four NVIDIA A100s run a calibration iteration on a dense-gauge twin 19× faster than a 64-core CPU socket.

For Hurricane Harvey on a 30 m mesh of the Houston area, roughness calibrated as well as we can calibrate it removes about 15% of the model's error against the surveyed high-water marks it was fit to. A scan of a single global roughness scale, forward runs alone, puts the reachable amount at 11%, and at 4% inside the prior, so the scale of the answer is known before any optimizer runs. The eigenvalues of the calibration problem at the published land-cover table show why so little is reachable: if that table is trusted to ±30%, the marks outweigh it on only about three combinations of its fifteen classes. Two of those three land in the same place under every prior we ran, below the table's own range for developed ground; the third goes where the prior lets it. The stream gauges cannot arbitrate between the survey and the table: most sit in channels the 30 m mesh does not resolve, and calibrating on the few it does leaves the model worse at the marks than no calibration at all. Roughness is absorbing whichever error each observable sees. Pointed at the initial state instead, the same measurement finds a larger effect: the model holds too much water when the window opens. The water balance and the mesh, not the friction, are where this error lives.

1 Introduction

Manning roughness is the dominant tunable parameter of depth-averaged flood models, and its calibration is traditionally manual or ensemble based. Adjoint methods deliver the gradient of an observation misfit with respect to *every* cell's roughness at a cost that does not grow with the number of parameters, a few forward solves as measured in Section 2.3, which makes distributed calibration tractable. The approach is well established in shallow-water modeling, from channel networks [1] and unstructured finite-volume twin experiments [2] to GPU-accelerated optimizers [3]. It is deployed in variational-assimilation platforms such as DassFlow [4, 5, 6] and the Thetis coastal

model, which calibrated a spatially varying Manning field for the Baltic Sea with an automatically generated adjoint [7], following storm-surge sensitivity studies that addressed the overfitting inherent in distributed friction estimation [8]. A newer route trains a physics-informed neural network on the observations and the equation residual and recovers the friction parameter with the fit; a benchmark on idealized steady channels with a single Manning scalar reports where it recovers the scalar and where it does not, under observation sparsity, noise and choice of observed variable [9]. The closest published work to ours is Pujol et al. [10], who infer distributed friction in a 2D urban flood model by variational assimilation of multi-source data including high-water marks, and who use adjoint-derived global sensitivity measures to decide how to spatialize the friction field before assimilating. Their observable is this paper's: surveyed high-water marks, the peak water levels a flood leaves on structures and debris lines, which we call the survey throughout. The design move is the same as well (Sections 6.1 and 6.2), at street scale and with a Tapenade-generated adjoint of a solver built for assimilation. What this paper adds is neither the adjoint nor the observable but the setting and the question: a production Earth-system component differentiated in place, and a measurement of how much of the model's error the parameter can explain at all with physically plausible roughness values. Roughness enters the model through a published table that assigns one Manning value to each of fifteen land-cover classes, and calibrating asks how far the survey can move those fifteen numbers. For this event and this observable no calibration we ran explains more than 15%, and reaching even that drives developed-medium land to the floor of the search, below anything the table assigns to any developed class. The spectrum of the calibration problem explains why so little of the error is reachable. If the table is trusted to about 30%, the marks are more informative than it is for only about three combinations of the fifteen, so calibrating three parameters recovers most of what calibrating all fifteen achieves. Trusting the table less does not increase how much of the error roughness can explain. It leaves the twelve combinations the marks cannot constrain with nothing to hold them but the bounds of the search, and the first step of a calibration drives seven of the fifteen classes to those bounds, reporting values that neither the table nor the survey supports. The measurement is not specific to roughness, and Section 7 turns it on the model's initial state, where it finds more.

A recent generation of *differentiable* flood and hydrology codes obtains gradients by rewriting simplified solvers inside machine-learning frameworks: Inunda (PyTorch, local-inertial, calibrated on a Hurricane Harvey hindcast) [11], Hydrograd (Julia) [12], AegirJAX [13], and differentiable routing [14]. These demonstrate demand for exactly this capability, but none is a production Earth-system component: they trade the validated numerics, unstructured meshes, and coupling infrastructure of codes like RDycore for differentiability. A parallel line ports production hydrodynamics to GPUs without differentiating them. CaMa-Flood-GPU [15] is a GPU reimplementation of CaMa-Flood, with gradient-based calibration named as future work rather than demonstrated.

This paper takes the complementary route: make the production code differentiable. That route has a long precedent outside E3SM. The most prominent is MITgcm, whose exact adjoint is generated by automatic differentiation of the production ocean model [16] and underpins two decades of global ocean state and parameter estimation in ECCO, Estimating the Circulation and Climate of the Ocean [17]. Ours differs in how the derivative is obtained rather than in ambition: the Jacobian is hand-differentiated and assembled, which makes it available to the implicit solver as well as to the adjoint, and Section 4 argues that for a differentiable friction term the implicit solve is not optional. Inside E3SM the precedent is narrower. The land-ice component MALI [18] routinely inverts for basal friction with an adjoint obtained by automatic differentiation of its Albany velocity solver [19], but that is the adjoint of a *steady* nonlinear solve, used for initialization. No E3SM component has, to our knowledge, a discrete adjoint of its transient time stepper. RDycore is a finite-volume shallow-water dynamical core (Roe fluxes, well balancing, wetting and drying)

validated at up to 471M cells [20]. We add the missing derivative infrastructure, an exact assembled Jacobian and TSAdjoint-based sensitivities [21], entirely behind a configuration flag, with no impact on existing runs and no new dependencies.

This paper contributes:

- a production Earth-system component differentiated in place: one exact, assembled Jacobian of the shallow-water right-hand side that serves the implicit integrator, the discrete adjoint and the calibration, gated against finite differences in continuous integration and resident on GPUs, with an objective and its gradient costing about 2.1 forward solves independent of the number of parameters; and the measurement that the explicit friction term cannot take a step on the 30 m Hurricane Harvey mesh, so the implicit solve is not optional (Sections 2 and 4);
- a measurement of how much of a flood model's error its roughness parameter is able to remove: about 15% of a 0.72 m survey error for this event by calibration, 11% by a forward-only scan of a global scale, against more for the initial condition (Sections 6.2, 6.3 and 7);
- the spectrum of the prior-preconditioned Gauss–Newton Hessian, a linearization at the lookup that counts the roughness combinations on which the observations outweigh the prior: about three of fifteen at a ±30% prior, and a three-class calibration that recovers 84% of the fifteen-class error reduction and lands below the lookup's own range for developed ground (Sections 5 and 6.4);
- a cross-observable test the stream gauges cannot arbitrate: 99.5% of their misfit at the lookup is a constant per-gauge level error, and a calibration on them moves two of the three classes against the marks and scores worse at the marks than the uncalibrated lookup, so the survey-only result is a fit and not a skill (Section 6.5);
- the identification of a downstream reach the model cannot drain, attributed to the closed catchment-divide perimeter of the domain under a storm that exceeded the divide, and of the water balance rather than the friction as where the remaining error lives (Sections 6.1 and 7).

2 Methods

2.1 Forward model

RDycore solves the 2D shallow water equations in conservative variables $u = (h, q_x, q_y)$, $\mathbf{q} = h\mathbf{v}$:

$$\partial_t h + \nabla\cdot\mathbf{q} = Q_r(x,t), \tag{1}$$

$$\partial_t \mathbf{q} + \nabla\cdot\Big(\tfrac{\mathbf{q}\otimes\mathbf{q}}{h} + \tfrac{gh^2}{2}\,\mathbb{I}\Big) = -\,gh\nabla z_b \;-\; g\,n^2 h^{-7/3}\,\mathbf{q}\,\|\mathbf{q}\|, \tag{2}$$

with cell-centered finite volumes on an unstructured mesh:

$$\frac{du_i}{dt} = -\frac{1}{|\Omega_i|}\sum_{e\in\partial\Omega_i} \mathcal{F}\big(u_i, u_j, \mathbf{n}_e\big)\,L_e + S(u_i; n_i, t) \equiv f_i(u, n), \tag{3}$$

where $\mathcal{F}$ is the Roe flux with a critical-flow (entropy) fix, primitives are reconstructed with a regularized division and a dry cutoff $h_{\min}$, and S contains bed slope, Manning drag, and external forcing.

The Roe flux's dissipation is built from the moduli $|\lambda_p|$ of its characteristic wave speeds, so the closed-form expression it evaluates switches wherever a wave speed changes sign. Switches like this, *branches* in the sense that $|x|$ has a positive and a negative branch, recur throughout the discretization. They belong to the model rather than to the derivative: a nonlinear solver must accommodate them whether or not anyone differentiates the code, which is the argument of Section 4. Away from a switching surface the map is smooth and equals its active branch; the derivative machinery of Sections 2.2.1–2.2.2 is *branch-faithful*, differentiating the expression the condition actually selected to give the correct one-sided derivative.

A differentiable right-hand side. RDycore's existing friction treatments (a semi-implicit splitting and the implicit scheme of Xia and Liang [22]) embed the time step, and in the semi-implicit case the flux divergence, inside the RHS callback. The resulting map is consistent only with forward Euler and admits no well-defined $\partial f/\partial u$. We therefore added a plain explicit source treatment (`source.method: explicit`), used on every adjoint path, and Section 4 shows how the implicit integrator, rather than the right-hand side f, then handles the resulting stiffness.

2.2 Differentiating the production solver

Two design decisions shape everything downstream. We obtain the derivative of the right-hand side by hand, as forward-mode differentiation of the flux computation itself, branch by branch, and we *assemble* it into a sparse matrix rather than apply it matrix-free. Assembly is what lets one artifact serve three consumers: the implicit solver preconditions with it (Section 4), `TSAdjoint` transposes it, and the calibration couples it to the parameter Jacobian. The two parts below build that Jacobian (Section 2.2.1) and the adjoint sensitivities on top of it (Section 2.2.2); every derivative is gated by finite differences of the full nonlinear solve.

2.2.1 Exact Jacobian

The RHS Jacobian is block sparse with 3×3 blocks on the cell-adjacency graph: each interior edge (i, j) contributes $\mp(L_e/|\Omega_{i,j}|)\,\partial\mathcal{F}/\partial u_{L,R}$ to the two cell rows, local sources contribute diagonal blocks, and boundary edges contribute diagonal blocks through the ghost-state map of the boundary condition.

Edge orientation is a classical source of sign errors in this construction, so one consequence of that structure needs stating. The pair $(\partial\mathcal{F}/\partial u_L, \partial\mathcal{F}/\partial u_R)$ is evaluated *once* per edge, in the edge's own stored normal direction, and then scattered to both cell rows with opposite area weights $-L_e/|\Omega_i|$ and $+L_e/|\Omega_j|$: the downwind cell receives the same two blocks with the roles of u_L and u_R exchanged between diagonal and off-diagonal positions. The normal is never flipped and the flux routine is never re-entered with reversed arguments, so conservation is structural rather than something the signs must reproduce, mirroring how the right-hand side itself accumulates the flux. The assembled-matrix checks in Table 1 would expose any lapse regardless, since they compare the full assembly against a matrix-coloring finite-difference Jacobian of the actual RHS on unstructured meshes with mixed boundary conditions, where a single mis-oriented edge is visible.

Flux blocks by forward-mode differentiation. Rather than deriving the dissipation-matrix derivatives symbolically, we differentiate the flux *computation*: a hand-written forward-mode (tangent) version of the Roe flux routine propagates directionals through every intermediate (Roe averages, eigenvectors, eigenvalues including both branches of the critical-flow fix, wave strengths, and physical fluxes), taking the code's own branch at every $|\cdot|$ and switch. The result is a consistent

Check	Configuration	Result	Gate
Edge flux blocks	wet jump 10 m/5 m	7.6×10^{-9}	10^{-6}
Edge flux blocks	transcritical (entropy-fix branch)	2.4×10^{-10}	10^{-5}
Source block	shallow flowing state	$< 10^{-6}$	10^{-6}
Assembled matrix	uniform flow, reflecting BCs	1.6×10^{-8}	10^{-6}
Assembled matrix	dam break, reflecting BCs	1.5×10^{-8}	10^{-6}
Assembled matrix	dam break, Dirichlet + critical outflow	1.9×10^{-8}	10^{-6}
dJ/du_0 (explicit RK)	8 sampled components	1.0×10^{-8}	10^{-5}
dJ/dn (explicit RK)	domain aggregate	2.9×10^{-6}	10^{-5}
dJ/du_0 (backward Euler)	tight inner tolerances	1.4×10^{-8}	10^{-5}
dJ/dn (backward Euler)	tight inner tolerances	5.3×10^{-6}	10^{-5}

Table 1: Relative errors of analytic derivatives against central finite differences of the full nonlinear computation. Every check in this table is an automated test in RDycore's `ctest` suite, run on every change to the repository.

one-sided derivative. Seeding unit directions through the primitive-reconstruction chain rule yields the two conservative-space blocks in six tangent evaluations per edge. The tangent code mirrors the flux code line by line, so it can be reviewed against it.

Boundary blocks. For a boundary edge, $F(u_{\text{in}}, u_g(u_{\text{in}}))$ contributes $(\partial_L F + \partial_R F\, \partial u_g/\partial u_{\text{in}})$. The reflecting map is a linear mirror; Dirichlet ghosts are constant; critical outflow has a closed-form ghost map $h_g = (q^2/g)^{1/3}$ with the code's inflow branch producing an identically zero flux.

Parameter Jacobian. Manning n appears only in the drag term, so $\partial S_{\mathbf{q}}/\partial n = -2gnh^{-7/3}\mathbf{q}\|\mathbf{q}\|$: two nonzeros per cell, supplied to `TSSetRHSJacobianP`.

Verification. Three layers, all against central finite differences, with the pass/fail tolerances fixed in advance of the runs (Table 1): an edge-level harness that differences the flux routine itself on sampled states (with a Richardson self-check of the FD order); full-matrix comparisons of the assembled Jacobian against a matrix-coloring FD Jacobian of the actual RHS on three state/boundary combinations, boundary rows included; and end-to-end gradient checks through the adjoint (Section 2.2.2). A finite-difference coloring Jacobian (`numerics.jacobian: fd`) remains available permanently as the verification baseline.

2.2.2 Adjoint sensitivities

For gauge observations y_k at times t_k with observation operator H (one row per gauge, selecting water height) and error variance σ^2,

$$J(n) = \tfrac{1}{2\sigma^2} \sum_k \|Hu(t_k) - y_k\|^2. \tag{4}$$

`TSAdjoint` [21] differentiates the discrete time stepper, so gradients are exact to roundoff for the computed trajectory, which is the property that makes the FD gates in Table 1 meaningful. Multi-time observations are handled by a segmented backward sweep: the adjoint is advanced between observation times with `TSAdjointSetSteps` and receives a jump $H^T\sigma^{-2}r_k$ at each t_k (Algorithm 1 in Section 2.3). One sweep yields both dJ/du_0 (state sensitivity) and dJ/dn (per-cell parameter gradient, via the two-nonzero parameter Jacobian).

Two integrator facts constrain the design. PETSc's plain forward-Euler integrator implements no adjoint, so the explicit adjoint-path configurations use the Runge–Kutta (RK) family. And for implicit integrators the discrete-adjoint gradient is only as exact as the inner solves: the Manning gradient fails its gate at default inner tolerances and passes once they are tightened (Table 1, implicit rows). We found loose inner tolerances a false economy on this problem: a tighter Krylov tolerance makes the implicit forward *faster*, because better linear solves let Newton converge in fewer iterations, and the production setting (Krylov 10^{-4}, nonlinear 10^{-5}) reproduces the fully converged answer to every printed digit for about 25% more wall time than the loosest usable setting. Campaigns therefore run at converged inner tolerances, and the verified gradients *are* the production gradients.

The peak observable. The real survey of Section 6.1 records event maxima rather than stage series, so every real-data number in this paper is scored on a peak. The misfit compares each mark cell's peak simulated water-surface elevation (WSE) over the window, $\max_k Hu(t_k)$, against the surveyed value, with H now selecting the mark cells. Its adjoint needs no new machinery: each mark's residual is injected at the time of its own peak, the argmax, in the segmented backward sweep of Algorithm 2. That is the exact gradient wherever the peak time is locally constant, and the parameter gradient of the peak misfit passes the same central-difference gates as every other block on the smooth verification twin of Section 3.

At basin scale the naive check fails, and a set of instrumented measurements pins down why, in a way that validates the gradient rather than the check (Table 2). No mark's argmax moves and none flips wet/dry across any probe, so the discrepancy lives below the observable. The evaluations are deterministic to nine digits, and in the domain-wide direction the FD value is stable across a decade of probe step (10^{-3} to 10^{-4} in α) while sitting 7.5% from the adjoint, which excludes noise, curvature truncation, and sparse kinks. Decisively, the gap accumulates with trajectory length: at the shortest window the gate passes at the inner-solve floor with every piece of machinery engaged, and it grows three orders of magnitude by basin window lengths. A proportional defect in $\partial f/\partial n$ or in the adjoint accumulation would err by the same fraction at any window length. Branch crossings accumulated along the trajectory, where the probe shifts which cells cross the depth cutoff at some step, predict exactly this profile.

Two further checks close it. Taking the probe a further decade down, to 10^{-5}, every direction falls toward the adjoint, the domain-wide one from 7.5% to 4.4% and the single-class directions faster, and developed-high passes the 10^{-5} gate outright there. And the fifteen per-class gaps sum to the domain-wide gap, the additivity that independent per-cell branch crossings predict and no plausible defect would arrange. We conclude that the adjoint returns the exact one-branch derivative. Over long windows the objective is dense with wet/dry branch surfaces, and a finite-step central difference converges to a locally smoothed slope that sits several percent from any one branch. The quasi-Newton iteration consumes one-branch derivatives of a piecewise-smooth objective, which is standard practice for max-type and switching systems, and its observed descent (Section 5.1) is consistent with that footing.

2.3 The calibration algorithm: strong-constraint 4D-Var

The complete calibration loop is summarized in Algorithms 1 and 2. It is a strong-constraint 4D-Var iteration, the variational form of data assimilation in which a misfit summed over a time window is minimized by a gradient method with the model enforced exactly, so the only controls are the Manning field and, optionally, the initial state. Each objective evaluation performs one checkpointed forward sweep (the trajectory is stored at a subset of steps and recomputed between

Window	Steps	FD-vs-adjoint gap, domain-wide direction
smooth verification twin	40	9×10^{-7} (gate 10^{-5}: pass)
basin, 1 min	60	9×10^{-5} (inner-solve floor: pass)
basin, 5 min	300	8×10^{-3}
basin, 15 min	900	2×10^{-2}
basin, 30 min	1800	2×10^{-1}
basin, 1 h	3600	7×10^{-2}

Table 2: The FD gate's failure accumulates with trajectory length on identical basin, rain, marks, and converged tolerances, the signature of branch crossings along the trajectory and not of gradient error. The 30-minute and 1-hour rows sample peaks over different horizons, so strict monotonicity across them is not expected; single-class directions sit one to three orders lower at every window.

them when the backward sweep needs it) that records the gauge residuals r_k at the observation times, followed by one backward sweep of the discrete adjoint (Algorithm 2). The per-iteration cost is therefore one forward sweep, the checkpoint recomputation the backward sweep requires, and one adjoint sweep, about 2.1 forward solves in total at production settings (Eq. (5)) and independent of the number of parameters. We measure that constant rather than assume it, since for a nonlinear model on a memory-limited device the checkpointing scheme, not the adjoint, sets it. Throughout, the objective splits as $J = J_{\text{mis}} + J_{\text{prior}}$, where the *misfit* $J_{\text{mis}} = (2\sigma^2)^{-1} \sum_k \|r_k\|^2$ measures disagreement with the observations and J_{prior} is the Tikhonov term of Eq. (6), a quadratic penalty on departure from the prior field. Only J_{mis} needs the adjoint; the prior term's gradient is closed form.

The backward sweep carries two vectors. The *adjoint state* λ holds $\partial J_{\text{mis}}/\partial u(t)$ at the current point of the traversal: seeded with the terminal observation sensitivity, propagated by the transposed Jacobian of the forward step map, and incremented by a jump $\sigma^{-2} H^T r_k$ at each observation time. The *parameter sensitivity* μ accumulates $(\partial \Phi_s/\partial n)^T \lambda$ at every step and is the complete misfit gradient dJ_{mis}/dn when the sweep reaches $t = 0$. Both transposed Jacobians are the analytic operators of Sections 2.2.1–2.2.2, applied within `TSAdjoint`'s discrete adjoint of the chosen integrator.

The outer update is BLMVM [23], the bound-constrained limited-memory quasi-Newton method of PETSc's optimization component TAO: a projected L-BFGS step with a backtracking line search, each trial point costing one forward-plus-adjoint evaluation. The loop terminates on the standard bound-constrained test: the projected gradient g^P (the gradient with components pointing out of the feasible box zeroed) drops below an absolute tolerance, or an iteration budget is reached. The same loop serves every parameterization in this paper: per-region, per-cell, and land-cover-class fields differ only in the expansion of the parameter vector onto cells (line 3 of Algorithm 1) and the corresponding summation of μ back onto parameters.

What a gradient actually costs. The textbook statement that an adjoint gradient costs "about one extra forward solve" assumes the forward trajectory is available to the backward sweep. For a nonlinear model it is not: the trajectory must be stored or recomputed, and at basin scale on GPUs it cannot be stored. Checkpoint recomputation is therefore a real and unavoidable term, and we measure it rather than assert it. On a one-simulated-hour window of the 2.93M-cell mesh (3,600 implicit steps at $\Delta t = 1\,\text{s}$, 400 in-memory checkpoints, four A100 GPUs on one node) a forward step costs 62.9 ms and an adjoint step 14.8 ms, and the backward sweep triggers 3,199 revolve recomputation steps, 0.89 of an additional forward. One objective-plus-gradient evaluation

Algorithm 1 Strong-constraint 4D-Var calibration of the Manning field, as implemented with TAO/BLMVM and `TSAdjoint`. The window map $M_{t_{k-1}\to t_k}$ is the composition of m steps of the discrete forward stepper (explicit RK, backward Euler, or ARK-IMEX).

Require: prior/initial guess n_0, bounds $[n_{\min}, n_{\max}]$, observations y_k at times $t_k = k\,m\,\Delta t$ ($k = 1, \dots, K$), gauge operator H, error σ, Tikhonov weight β, gradient tolerance ε_g, iteration budget $I_{\max}$

$n \leftarrow n_0$
repeat
  set the model's cellwise drag coefficient from n ▷ identity for per-cell n; constant over each region or land-cover class for the reduced parameterizations
  $u \leftarrow u_0$ ▷ fixed initial state (strong constraint)
  for $k = 1, \dots, K$ **do** ▷ forward sweep; trajectory checkpointed — every step, or a revolve schedule for long windows (Section 4)
    $u \leftarrow M_{t_{k-1}\to t_k}(u;\, n)$
    $r_k \leftarrow Hu - y_k$
  end for
  $J \leftarrow \dfrac{1}{2\sigma^2}\sum_{k=1}^{K}\|r_k\|^2 + \dfrac{\beta}{2}\|n - n_0\|^2$
  $(\lambda, \mu) \leftarrow$ AdjointSweep$(\{r_k\})$ ▷ Algorithm 2 differentiates the stepper above, so $\mu = dJ_{\mathrm{mis}}/dn$ is exact to roundoff and inner-solver tolerance (Section 2.2.2)
  $g \leftarrow \mu + \beta\,(n - n_0)$
  $n \leftarrow$ one projected BLMVM step from (n, J, g) ▷ clipped to $[n_{\min}, n_{\max}]$
until $\|g^P\| \le \varepsilon_g$ or $I_{\max}$ iterations
return n

Algorithm 2 AdjointSweep: segmented discrete-adjoint backward sweep (`TSAdjointSolve` with `TSAdjointSetSteps`). Φ_s denotes the forward map of step s, $u_s = \Phi_s(u_{s-1}; n)$; its transposed Jacobians are built from the assembled RHS Jacobian $\partial f/\partial u$ (Section 2.2.1) and the parameter Jacobian $\partial f/\partial n$ according to the integrator's discrete-adjoint formula.

Require: checkpointed trajectory $\{u_s\}_{s=0}^{K\,m}$, residuals $\{r_k\}_{k=1}^{K}$ at steps $s = k\,m$, gauge operator H, error σ; as in Algorithm 1, m is the number of steps between consecutive observation times, so the window is $K\,m$ steps long

Ensure: $\lambda = dJ_{\mathrm{mis}}/du_0$, $\mu = dJ_{\mathrm{mis}}/dn$

$\lambda \leftarrow \sigma^{-2} H^T r_K$ ▷ λ holds $\partial J_{\mathrm{mis}}/\partial u(t_s)$ throughout
$\mu \leftarrow 0$
for $s = K\,m, \dots, 1$ **do**
  restore u_{s-1} (and stage values): read the checkpoint, or recompute forward from the nearest one when the checkpoint schedule demands
  $\mu \leftarrow \mu + \left(\partial\Phi_s/\partial n\right)^T \lambda$ ▷ accumulate this step's Manning dependence
  $\lambda \leftarrow \left(\partial\Phi_s/\partial u_{s-1}\right)^T \lambda$ ▷ backward model step (transposed step Jacobian)
  if $s - 1 = k\,m$ for some $1 \le k < K$ **then**
    $\lambda \leftarrow \lambda + \sigma^{-2} H^T r_k$ ▷ observation jump: $u_{k\,m}$ enters J_{mis} directly
  end if
end for
return (λ, μ)

is thus

$$\underbrace{1.00}_{\text{forward}} + \underbrace{0.89}_{\text{recomputation}} + \underbrace{0.24}_{\text{adjoint sweep}} \approx 2.1 \text{ forward solves}, \tag{5}$$

about nine minutes on that node. Note where the cost sits: the adjoint sweep itself is the *cheapest* of the three terms, and recomputation is the expensive one, so the ratio is a property of the checkpoint budget rather than of the adjoint. More checkpoints buy less recomputation until device memory runs out, and the 400 used here are near optimal for this step count. What does *not* change with the parameter count is the whole of Eq. (5): the same 2.1 forwards deliver a gradient with respect to one parameter or to 2.93 million, which is the property that makes distributed calibration tractable.

Each trial step of the BLMVM line search costs one such evaluation. A basin-scale window needs more iterations than a single batch allocation provides, so a run writes its parameter vector on exit and the next reads it back as its starting iterate, matched by land-cover class rather than by position. The resume is exact in the parameters (the continuing run's first objective reproduces the previous run's last to six digits), but BLMVM's stored curvature pairs do not survive it, so a chain of jobs is not step-for-step identical to one long run.

Scaling the calibration problem. A quasi-Newton method needs its variables and its objective to be $O(1)$, and in physical Manning units this problem is not: on a 600-step window of the production configuration $\|g\| \approx 1.5 \times 10^3$ while $n \approx 0.05$. Starting from $B = I$, the first trial point $n - g$ therefore projects every component onto the lower bound, where the model cannot solve (a uniform $\alpha = 0.2$ diverges, Table 9), so every line-search trial fails and the optimizer returns having taken no step. The failure presents as a solver defect: nothing is wrong with the gradient, and the finite-difference gates pass throughout.

Two changes make the problem well scaled, and both have physical readings rather than being tuning constants. First, optimize the *relative* field $\alpha_k = n_k / n_{\text{prior},k}$ and the relative objective $J/J(n_{\text{prior}})$. Here and throughout, α is a multiplier on roughness, never a step length: a class at $\alpha = 1.5$ carries 1.5 times its lookup value, and the uniform scans of Section 6.2 set every class to the same α. Both are then $O(1)$ and the unit quasi-Newton step becomes a roughness change of order 10%: at the start point of the production configuration, the National Land Cover Database (NLCD) lookup, over a shortened window that reproduces the zero-step failure exactly, $\|g\|/J_0 = 0.10$, and the same start point that took no step in physical units takes one that lowers the objective and the mean absolute error (MAE) of the peak WSE together. The bounds become statements about relative roughness, $\alpha \in [0.3, 3]$, which additionally excludes the region where the implicit solve fails. Second, set the Tikhonov weight from a prior standard deviation on Manning n rather than by hand,

$$J = \underbrace{\frac{1}{2\sigma^2} \sum_k \|r_k\|^2}_{J_{\text{mis}}} + \underbrace{\frac{\beta}{2} \|n - n_{\text{prior}}\|^2}_{J_{\text{prior}}}, \qquad \beta = \sigma_n^{-2}, \tag{6}$$

and report σ_n. This matters because β is dimensional: a bare value is uninterpretable across problems, and ours had been chosen independently in every experiment, spanning nearly ten orders of magnitude. Against the measured $J(\alpha)$ curve, $\sigma_n = 0.015$ places the minimum of the uniform-scaling direction at $\alpha \approx 0.70$, while $\sigma_n = 0.020$ leaves no interior minimum there at all, the same pathology the hand-chosen weight had. We ran the scan point at $\alpha = 0.70$ afterwards and measured an MAE of 0.6894 m against the 0.6895 m the balance implied (Table 9). Stating the prior turns the choice into an arithmetic consequence of a stated uncertainty on Manning n.

Configuration	Mesh	Window	Observable	Parameters
Verification twin	planar, two regions	1.8 s, 40 steps	water height	per-cell, per-region
Houston twin	1 km, 2,746 cells	4200 s, $\Delta t = 30$ s	343 or 686 gauges, 14 times	2,746 per-cell
Houston, real network	1 km, 2,746 cells	4200 s, $\Delta t = 30$ s	17 USGS gauges, 238 obs	2,746 per-cell
Turning, class twin	30 m, 2.93M cells	early transient	13 gauges, 260 obs	15 NLCD classes
Turning, dense twin	30 m, 2.93M cells	early transient	418,076 strided cells	15 NLCD classes
Turning, mark twin	30 m, 2.93M cells	1 h, rain-forced	108 marks, peak WSE	15 NLCD classes
Turning, full event	30 m, 2.93M cells	72 h, $\Delta t = 1$ s	108 marks, peak WSE	forward only
Turning, production	30 m, 2.93M cells	12 h, event h29–41	46 marks, peak WSE	global scale, 15 classes

Table 3: The configurations used in Sections 4–7. Every row above *Turning, full event* is a twin, observing model output generated from a roughness field we chose. The twins are part of the argument rather than preparation for it: a recovered field can be scored only against a known truth, and that score is what separates *this observable cannot determine the parameter* from *the derivative is wrong*. The real survey admits no such check, so the twins are what license reading Sections 6–7 as statements about information rather than about correctness. The last five rows are the 30 m Hurricane Harvey domain, where the observable changes from stage gauges to surveyed high-water marks for the reason given in Section 6.1. Every number reported against the real survey (baseline, scans, calibration, and spectrum) is measured on the production row, so those results compose.

Absolute or fractional prior. Equation (6) states the prior as an absolute departure in n, and for a land-cover table that is the wrong statement. A single $\sigma_n = 0.015$ over an NLCD lookup spanning $n = 0.027$ (barren) to $n = 0.16$ (developed high) asserts a $\pm 56\%$ prior on one class and $\pm 9\%$ on another. Because the penalty scales as n_{prior}^2, a small-n class buys a large *fractional* excursion cheaply. Penalizing the fractional departure $n_k / n_{\text{prior},k} - 1$ with a width σ_α instead treats the classes alike, and states the prior as the percentage by which the lookup can be wrong.

Which width to state is a judgment about the land-cover lookup rather than a tuning parameter, so we report the width used with every number. Whether the reformulation relieves the tension is a result and not an implementation detail, and Section 6.3 measures it.

The failure mode is not specific to this model: an optimizer that takes zero steps on a problem whose gradient passes every verification gate is a scaling defect, and the cheapest test is to compare $\|g\|$ against the scale of the variable before suspecting the derivative.

3 Model configurations

The results that follow run the machinery of Section 2 on three domains, at resolutions a factor of 30 apart and against four different observables. Because the paper's central claim is comparative (what a parameter can explain *on a given observable and window*), the configuration is part of every result rather than background to it. Table 3 collects the configurations so that later sections can name one instead of restating it.

The twins. The verification twin is a planar, 40-step configuration whose only purpose is to exercise the derivative machinery where the objective is smooth; it carries the finite-difference gates of Table 1 and the noise study of Table 5. The Houston twin is a 1 km Hurricane Harvey mesh of 2,746 cells in which every cell is wet and moving, so all 2,746 per-cell parameters are observable in principle; truth is a two-zone field ($n = 0.03$ west, $n = 0.06$ east of the domain midline) and the recovered field is scored against it. Its real-network variant replaces the synthetic

gauges with the seventeen in-mesh U.S. Geological Survey (USGS) gauges carrying Harvey stage records.

The 30 m Harvey domain. The Turning mesh resolves the Houston area at 30 m in 2.93M cells, with one Manning value per NLCD land-cover class (15 classes) and the published NLCD lookup as both prior and, for twins, truth. Four calibration configurations and the 72-hour forward of Section 6.1 share it. The class and dense twins ask whether fifteen classes are identifiable, that is, recoverable from the observations alone, from the real gauge geometry and from a saturating observation set respectively. The mark twin replaces stage with peak water-surface elevation at the 108 high-water-mark cells that pass the quality control (QC) of Section 6.1. The production configuration is the one every real-survey number is measured on: a 12-hour window over the upstream crest cluster, event hours 29–41 counted from the start of the 72-hour forward of Section 6.1, initialized from an hourly checkpoint of that forward with the rain re-aligned to the window start (both validated bit-exactly), scored against the 46 surveyed marks whose modelled crest falls inside it. Section 6.2 explains why the observable, not the budget, sets that window.

Shared solver settings. Every adjoint-path configuration uses the explicit source treatment (`source.method: explicit`) with stiffness handled by the implicit integrator rather than inside the right-hand side (Section 2.1), and runs at converged inner tolerances (Krylov 10^{-4}, nonlinear 10^{-5}) so that the verified gradients are the production gradients (Section 2.2.2). Calibrations use TAO/BLMVM: the per-cell twins bound n to $[0.01, 0.2]$, the class twins to $[0.005, 0.30]$, and the class calibrations against the real survey bound the relative field to $\alpha \in [0.3, 3]$ (Section 2.3). Long windows use revolve checkpointing (Section 4).

4 Implicit stepping, enabled and required

The explicit drag term is stiff in thin water: its linearized rate is $gn^2h^{-4/3}|v|$, so an explicit step must stay below the inverse rate, $\Delta t \lesssim h^{4/3}/(gn^2|v|)$, seconds for sheet flow at centimeter depths, against the 30 s gravity-wave step of the 1 km mesh. On the Houston 1 km configuration ($\Delta t = 30$ s) we found the explicit source treatment returns a non-finite state within the first objective evaluation, as the estimate predicts. The same holds at basin scale, where the margin is a factor of 400: on the spun-up 30 m, 2.93M-cell Harvey mesh (99.9% wet, median depth 6 mm) the stiffest cells reach a friction rate of $420\,\mathrm{s}^{-1}$, so $\Delta t \lesssim 2.4$ ms, and 90k cells violate that limit at $\Delta t = 0.25$ s; forward Euler of the differentiable right-hand side returns a non-finite state at every tested step ($\Delta t = 0.25$, 0.125, 0.05 s) while backward Euler at $\Delta t = 1$ s completes a 72-hour window without a Newton failure. There is no viable explicit path for the differentiable right-hand side at this resolution.

The assembled exact Jacobian supplies the remedy directly: backward Euler via PETSc's theta method, with SNES driven by the same Jacobian, carries the 1 km Houston window at $\Delta t = 30$ s and the 30 m mesh at $\Delta t = 1$ s, and the theta-method adjoint passes the same FD gates (Table 1).

An ARK-IMEX splitting with the Manning drag as the stiff implicit part is also implemented (`temporal: arkimex`); its implicit stage system is block-diagonal, an independent 3×3 Newton per cell, and its adjoint passes the same gates. No production number in this paper uses it.

Newton robustness is set by residual discontinuities, not by conditioning. Where implicit stepping fails on this problem, it fails for a reason that is invisible in the smooth twin experiments: the residual is discontinuous, so Newton has nothing to converge *to*. At the land-cover roughness prior, rather than the twins' smooth low-n fields, backward Euler descends for a

Rain-forced configuration (land-cover prior)	Outlet	Outcome
600-step control	critical outflow	Newton pinned from step 498
600-step control	free outflow	zero failures; 598/600 solves in two iterations
1-h calibration window (forward + adjoint + line search)	free outflow	clean end to end
72-h forward through the Harvey crest (2.93M cells)	free outflow	259,200 solves, zero failures

Table 4: The outlet replacement is a cure, not an improvement. Under critical outflow, tolerance relief bought steps only linearly; the transmissive outlet completes the identical window and every longer one attempted.

dozen iterations and then stalls: a line-search step of negligible length changes the residual norm severalfold, which is the signature of a jump, not of ill-conditioning. Two mechanisms are responsible, both invisible until the parameter field is realistic: the drag's wet/dry cutoff, whose amplitude scales as n^2, and the critical-outflow boundary's stagnation switch. Both are discontinuities of the residual rather than of its derivative, and both are removed by changing the model rather than the solver. The drag $gn^2h^{-7/3}\mathbf{q}\|\mathbf{q}\|$, gated at the dry cutoff with a plain $\mathbf{q}/h$ velocity, switches an $O(h^{-7/3})$ term on and off as a cell crosses the cutoff; evaluating it with the regularized velocity $\mathbf{u} = \mathbf{q}h/(h^2 + h_{\text{anuga}}^2)$ of ANUGA, with $h_{\text{anuga}} = 0.001\,\text{m}$, makes the drag vanish as $h^{5/3}$ instead and reduces to the plain form at $h_{\text{anuga}} = 0$. The value is the smallest that removes the stall: 0.003 m is indistinguishable from it and 0.01 m is unstable. The outflow condition is replaced in the same spirit.

Both fixes are implemented, gated, and opt-in. Regularizing the drag velocity removes the first and restores convergence over the early transient. The second we removed by replacing the outlet condition itself: a transmissive (zero-gradient) free outflow, in which the ghost state copies the interior state (the convention of most finite-volume shallow-water codes), is continuous in the interior state by construction, and its ghost map is the identity, so the analytic Jacobian and adjoint carry it exactly, FD-gated like every other block. The effect on the solver is not an improvement but a cure (Table 4): the identical failing control completes with zero nonlinear failures, and the fix holds through the longest windows we run. The cure has a cost that critical outflow did not: the transmissive condition carries no inflow guard, so an outlet whose interior momentum points inward admits water, and Section 6.1 measures how much the production forward admitted. Before the replacement we absorbed the stall by loosening the nonlinear tolerance, and a class-twin calibration under that setting still recovered all fifteen class values to machine precision, so the gradient path was unimpaired. The general lesson for adjoint retrofits is that nonsmoothness in an operational flood code is a nonlinear-solver question as well as a differentiability question.

Checkpointed adjoints for long windows. A stored trajectory for a full 36-hour Hurricane Harvey window at the 30 m mesh's explicit gravity-wave (CFL) limit of $\Delta t = 0.25\,\text{s}$ (518,400 steps, 2.93M cells) would occupy tens of terabytes, far beyond device memory. PETSc's checkpointing trajectory (`-ts_trajectory_type memory` with the revolve optimal-schedule library) replaces storage with recomputation. We validated it across the full hierarchy. On the dam-break twin it reproduces the disk-trajectory calibration and gradient gates bit-for-bit for explicit RK, backward Euler, and ARK-IMEX (the implicit integrators need the same tight inner tolerances as in Section 2.2.2, since checkpoint recomputation re-solves the stage systems). On the 30 m mesh, a forward-plus-adjoint sweep with only *three* states checkpointed in memory matches the disk-trajectory gradient to all

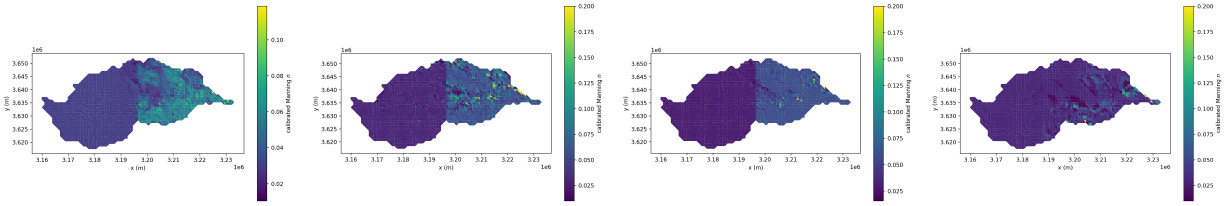


Figure 1: Regularization, semiconvergence, and network density on the Houston twin (2,746 parameters; truth: $n = 0.03$ west, $n = 0.06$ east of the midline; implicit stepping, 14 observation times). Far left: weak regularization ($\beta = 10^{-5}$, 343 gauges) stopped early at 300 iterations, 26.3% error. Center left: the same setup run to 2000 iterations; the misfit is lower but the field drifts along unobserved directions to 38.0% error and saturates the bounds $[0.01, 0.2]$. Center right: ten times the weight and twice the gauges ($\beta = 10^{-4}$, 686 gauges), 1000 iterations, 19.4% error, no drift, sharp zone boundary. Far right: the *real* network, the 17 in-mesh USGS gauges with Harvey stage records, same $\beta = 10^{-4}$, 1000 iterations; the misfit falls 2×10^7-fold while the field recovers to only 44.9%: no trace of the two-zone truth, near-prior almost everywhere with null-space structure pinned against both bounds.

printed digits, and runs faster (recomputation is cheaper than trajectory I/O at this scale). For the full window, a few hundred checkpoints (∼14 GB aggregate) bound the recompute overhead by a factor of about four, making the long-window adjoint memory-feasible; the remaining cost is the forward compute itself, measured in Eq. (5).

5 Twin experiments: what the observing network can recover

In a twin experiment the observations are model output generated from a roughness field we chose, so a calibration can be scored against a known truth rather than against a real survey whose own errors are unknown. The per-cell twin runs on the Houston 1 km Hurricane Harvey mesh (2,746 cells, 4200 s window at $\Delta t = 30$ s). Truth is the two-zone field of Section 3, observed at 343 synthetic gauges over 14 observation times, calibrated with implicit stepping and Tikhonov regularization ($\beta = 10^{-5}$). The configuration is deliberately gauge-sparse (343 gauges for 2,746 parameters) and shows the classic *semiconvergence* of underdetermined inverse problems, in which the recovered field first approaches the truth and then drifts away from it while the misfit keeps falling (Figure 1): at 300 BLMVM iterations the recovered map shows the two-zone truth at 26.3% relative L^2 error, and continuing the same weakly regularized optimization to 2000 iterations degrades it to 38.0% as the parameters drift along observation-null directions and pin against both bounds, early stopping having acted as the regularizer. A run with ten times the Tikhonov weight and twice the gauges ($\beta = 10^{-4}$, 686 gauges) reaches 19.4% at 1000 iterations with no drift. This is the overfitting risk documented for distributed friction estimation [8], reproduced in a controlled twin.

The real gauge network. The synthetic gauge sets above are a controlled ramp; the network that matters is the real one. Twenty USGS gauges fall inside the Houston mesh, seventeen with Hurricane Harvey stage records.[1] In the same twin with the observation operator built at those seventeen gauge cells (238 observations, 17 gauges × 14 times, against 2,746 parameters), BLMVM drives the misfit down by a factor of 2×10^7 (the synthetic observations carry no noise and are fit

[1] HydroShare DOI `10.4211/hs.c037167e497546a1bc1508dfb32a9cff`.

to roundoff) while the recovered field is 44.9% from the truth and saturates both bounds (Figure 1, far right). This is semiconvergence in its purest form: the real network's null space, the set of roughness changes it cannot see, is so large that data fit says almost nothing about parameter recovery, and no Tikhonov weight or stopping rule rescues a per-cell field from 238 observations. The practical conclusion for real-data calibration is to shrink the parameter space to match the network. Shrinking it is necessary and not sufficient, as the next subsection measures: whether a reduced parameterization is identifiable depends on the observation geometry and window, not on the ratio of observation to parameter counts.

5.1 Identifiability is a property of the observable: gauges versus high-water marks at 30 m

The natural reduced parameterization for this domain is one Manning value per NLCD land-cover class (15 classes at the 30 m Turning mesh, 2.93M cells), with the published NLCD lookup as prior and truth for twins. Counting favours it: even the sparse real network supplies an order of magnitude more observations than parameters. A twin shows otherwise. In a class twin on the 30 m mesh at the real 13-gauge geometry (260 observations, a short early-transient window), the objective falls 128× while the recovered class values remain 66% wrong in relative L^2, worst class 81%. The failure is structural: classes whose cells are dynamically distant from every gauge (the three forest classes) never move from the starting value, because within the window nothing their roughness does reaches a gauge. The identical configuration observed at 418,076 strided cells recovers all fifteen classes to machine precision, so the failure is the network, not the method. Fifteen parameters and thirteen gauges, an "overdetermined" observation count, remain unidentifiable.

The same question re-asked with the peak observable comes out differently. Observing the same NLCD-truth twin at the 108 QC-passed high-water-mark cells (peak WSE sampled over a one-hour rain-forced window, implicit stepping, free-outflow outlet; Section 6.1) and calibrating fifteen classes from a uniform start: the objective falls 81×, the peak-WSE error at the marks drops from 0.103 m to 0.017 m MAE, and the area-dominant classes are identified: the three developed-intensity classes, pasture, and crops recover to 0.7–10.5%, together 83% of the domain's cells, for an area-weighted relative L^2 error of 0.20 (unweighted 0.58). The residual errors concentrate in small-area classes (forests, shrub, emergent wetland, each under 3% of the domain's cells), which now *move* (they are sensitive, unlike in the gauge experiment) but overshoot to the bounds along weakly constrained directions. That is ordinary semiconvergence, treatable with regularization and longer windows, rather than a structural absence of signal. Three caveats apply: the one-hour window samples early-transient peaks, not flood peaks (the real calibration windows are 6–12 hours and should only help); the run was capped at 15 quasi-Newton iterations; and twin marks synthesized from the truth trajectory carry no representation error, the part of a model–observation mismatch that comes from comparing a point measurement with a cell average rather than from any error in the model's parameters, so this is an identifiability statement, an upper bound on real-data performance rather than a forecast of it.

Noise turns identifiability into a signal-to-noise question. Every recovery above is noise-free, as are the verification twins behind Section 2.3. Such experiments establish that the gradient is right and that the observable carries the information; they do not establish that a field can be calibrated from real data. What separates the two is the size of the parameter-induced signal relative to observation error, and that ratio moves by orders of magnitude with the configuration (Table 5). On a short verification window the entire Manning-induced observation signal is a few microns of water height, so a noise-free optimizer descends on it indefinitely while a tenth of a

Configuration	Signal	Observation noise	Outcome
Verification twin (planar, 40 steps, 1.8 s)	5 μm water height	none 0.1 mm 1 mm	per-region recovery 4×10^{-7} per-cell recovery destroyed (0.20 $\rightarrow$ 1.8) per-region destroyed ($4 \times 10^{-7} \rightarrow 0.83$, both at bounds)
30 m basin, 1 h	~ 0.1 m	none	area-weighted rel. L^2 0.20; MAE 0.103 $\rightarrow$ 0.017 m
rain-forced, 108 marks	peak WSE	0.15 m (HWM grade)	misfit falls 9.4$\times$, MAE 0.23 $\rightarrow$ 0.12 m — but 5 of 15 classes pin to bounds

Table 5: Parameter-induced observation signal versus observation error. The noise-free recoveries differ by four orders of magnitude in the signal they descend on; only the basin-scale row is a fair test against the 0.15 m survey-grade error used throughout. Noise is a deterministic, decomposition-independent perturbation of the twin observations, so the comparison is reproducible across rank counts.

millimetre of observation noise destroys the recovery outright, and the best Tikhonov weight in a sweep from $\beta = 10^{-4}$ to 1 leaves the per-cell error at 0.44, more than twice the noise-free 0.20. At basin scale the same quantity is ~ 0.1 m of peak water-surface elevation after one simulated hour, four orders of magnitude larger, which is the regime in which a parameter signal can exceed survey-grade high-water-mark error. The lesson is not that the method is fragile: it is that friction must act long enough to imprint a signal above the noise floor, which makes window length a first-class calibration decision rather than a cost parameter.

The basin-scale noisy row shows what marginal signal-to-noise looks like in practice, and why misfit at the marks is the objective but not the result. With 0.15 m of observation noise, even the *true* field cannot beat a mark MAE of about $\sigma\sqrt{2/\pi} \approx 0.12$ m against the noisy values, and the optimizer reaches that floor while driving five of the fifteen classes onto their bounds (pasture, 428k cells, to the ceiling) and ending far from the true field it was supposed to recover. The data fit is as good as truth could achieve; the parameters that achieve it are wrong, because the last of the misfit was removed by matching noise. On real data the parameter error is invisible and the bound-pinning is its symptom, which is the argument for stronger regularization, a longer window, and discrepancy-principle stopping (stop at the noise level rather than descend past it) in the production run.

6 The real survey: what roughness can explain

The twins establish what the machinery can recover under controlled conditions. This section turns it on the real Hurricane Harvey survey. The observable changes first, because the stage gauges are unusable at this resolution, and everything after that is measured against surveyed high-water marks: the uncalibrated baseline and the drainage defect it exposes (Section 6.1), how much of the remaining error roughness can remove (Section 6.2), the calibration (Section 6.3), the spectrum that counts the parameter combinations on which the marks outweigh the prior (Section 6.4), and a validation of the calibrated field against the stream gauges, which fails (Section 6.5). Section 7 then points the same measurement at the initial condition.

Gauge	cell bed (m)	window WSE (m)	above bed
Buffalo Bayou nr Katy	33.27	35.58–36.05	100%
Buffalo Bayou at Houston	6.93	10.71–12.77	100%
Langham Ck nr Addicks	28.23	30.74–31.25	100%
Bear Ck nr Barker	34.73	34.87–34.94	100%
Buffalo Bayou nr Fulshear	31.47	31.23–31.56	29%
Langham Ck at W Little York	34.10	32.76–34.09	0%
S Mayde Ck	34.60	34.07–34.29	0%
Whiteoak Bayou at Alabonson	23.60	22.26–23.48	0%
Brickhouse Gully	20.40	16.24–19.64	0%
Cole Ck	25.30	20.95–22.47	0%
Little Whiteoak Bayou	14.50	10.65–13.37	0%
Whiteoak Bayou at Main St	11.80	9.71–11.33	0%
Whiteoak Bayou at Houston	15.03	no record in window	

Table 6: The 30 m mesh against the stage record at the thirteen rain-driven USGS gauges over the calibration window (event hours 29–41). Stage at these gauges is published as water-surface elevation (WSE) in NAVD88, the datum of the mesh, so the cell's mean bed elevation and the observed water surface compare directly. "Above bed" is the fraction of the window's 15-minute records with the observed water surface above the cell bed. At seven gauges the bed sits above even the window's peak stage: the cell holds the bank, and no roughness value places water in it at the elevation the gauge reads.

6.1 High-water marks and the uncalibrated baseline

Calibration against the actual stage records is blocked by geometry, not software. A 30 m cell stores one mean ground elevation, the bank of an incised bayou, while the gauge hangs in the channel below it. Comparing the mesh directly against the stage record makes the geometry explicit (Table 6): over the calibration window the cell bed sits above the *peak* observed water surface at seven of the twelve gauges with data, and above the water surface for 71% of all gauge records. Only the two Buffalo Bayou main-stem gauges, where the channel is wider than a cell, hold their water for the whole window; the two gauges in the Addicks and Barker reservoir pools hold it for every record they have, 20 and 4 of the 48 slots, and a fifth, Fulshear, for 29% of the window. Where the cell does hold water, the model runs one to five metres above the observed surface at four of those five gauges (Section 6.5 measures this gauge by gauge). The mesh resolves the major channel and not the tributaries, which is where all but the three Buffalo Bayou gauges sit.

We therefore changed the observable to the USGS high-water-mark archive: surveyed *peak* water-surface elevations on structures and debris lines, i.e. on the floodplain surfaces a 30 m cell does represent, and the benchmark currency of the flood-modeling literature (Inunda reports 0.67 m MAE against Harvey high-water marks [11]). Of 2,364 Harvey marks, 324 fall in the Turning domain. Applying to the marks the same QC that disqualified the gauges, whether the surveyed elevation lies above the containing cell's bed, rejects 62% of them (they are channel surveys), and keeping only survey quality fair or better leaves 108. The mismatch this QC addresses is the one Xu et al. measured on a 30 m simulation of the same event: validated against 48 marks, their simulation had an RMSE of 0.9 m with 25 of 48 within 25%, which they attribute to comparing a point survey with a cell average [24]. Two choices here reduce that exposure. The QC keeps only marks on surfaces a cell represents, and the misfit compares water-surface elevations rather than depths, so the difference between the ground at the point and the mean ground of the cell enters once, through the cell bed, and not a second time through the depth. The peak misfit and its

adjoint are those of Section 2.2.2. The remaining scientific choice is the calibration window, which for marks that record the event maximum must cover the flood peak.

The uncalibrated baseline against the real survey. Because the marks record the event maximum, the baseline evaluation must simulate through the crest: a 72-hour rain-forced forward from the available initial state (2017-08-26 18:00, reaching past the Buffalo Bayou crest), NLCD-prior Manning, free outflow, backward Euler at $\Delta t = 1\,\mathrm{s}$ on the 2.93M-cell mesh. That is 259,200 implicit steps with zero Newton failures, in two hours on one GPU node. The model wets all 108 marks, and the uncalibrated peak-WSE error separates into two populations (Table 7; confirmed mark for mark at fully converged inner tolerances). The 71 marks that crest inside the window carry the error a Manning field can plausibly address. The other 37 never crest. Their cells fill monotonically through the whole window, every one peaking at the final hour with zero recession, and accumulate some ten metres of standing water that arrives laterally after the rain has ended. Those cells sit in the downstream Buffalo Bayou reach, which the model cannot drain. No roughness value can absorb that, and a calibration asked to fit those marks would absorb the defect into the friction.

The exit is not missing. The domain is a delineated watershed rather than a rectangular cutout (35 of its 6,198 boundary nodes lie on the bounding box), so its untagged perimeter is a catchment divide and a reflecting wall is the right condition there. Its single free-outflow side set, thirteen element edges wide, sits at the perimeter's lowest point: the only boundary nodes at $z \approx 0$, against a boundary median of 29.9 m. What the ponded reach exposes is the idealization itself. The perimeter follows the real watershed boundary, and on this terrain such boundaries are crossed in storms far smaller than Harvey: Cypress Creek overflows overland into the Addicks and Barker watersheds, whose tributaries Bear, South Mayde and Langham Creeks are gauged in Table 6, in storms of five-year recurrence and above, and in a hundred-year storm 83% of its flood volume crosses that divide [25]. The documented crossing is an inflow at the upstream end of the domain, not an outflow at the ponded reach. That water also left the domain across the divide near the downstream reach in an event of Harvey's size is our reading of the event, not a measurement of this paper, and a closed boundary represents neither crossing.

The one boundary that is open is not a pure exit. The transmissive condition of Section 4 copies the interior state into the ghost cell, so the outlet passes whatever flux the interior momentum sends it, in either direction. Summing that flux over the thirteen outlet edges from the hourly checkpoints of the 72-hour forward, the outlet admits water for the first 38 hours, $8{,}500\,\mathrm{m^3\,s^{-1}}$ inward at hour 3 and about $1.9 \times 10^8\,\mathrm{m^3}$ by hour 29, which is 19% of the water the domain holds then, and discharges about $3.6 \times 10^7\,\mathrm{m^3}$ over hours 39–72, $660\,\mathrm{m^3\,s^{-1}}$ at hour 72. Over the event the only exit is a net source. Where the admitted water sits at hour 29, and whether any of it reaches the upstream band, we have not measured. What this paper measures at the marks is that the model retains water the survey did not record: every one of the 37 marks is model-high, by 7 m on average (Table 7). The calibration target is therefore the 71 marks that crest, narrowed further below; the drainage defect is a finding in its own right; and the remaining error bundle (initial-condition, rainfall, mesh-elevation, and datum error) is what the calibration must be prevented from absorbing along with the roughness signal.

The defect grows downstream rather than switching on. Sorting the marks by crest time splits them into three groups, and those groups turn out to be three *spatial bands* whose bias increases monotonically downstream (Table 8). The never-crest population is the end of a continuum, not a separate pathology: the intermediate band already carries +2.85 m of the same

Marks	n	MAE	bias
crest inside the 72-h window	71	1.51 m	+1.20 m
never crest (reach cannot drain)	37	7.06 m	+7.06 m
all	108	3.41 m	+3.21 m

Table 7: The uncalibrated baseline against the 108 surveyed high-water marks, decomposed. The second population is model-high at every single mark and identifies a reach the model cannot drain; the first is the calibration target.

Group	n	mean lon.	bias	MAE
crest h29–41 (upstream)	46	−95.695	+0.30 m	0.72 m
crest h48–72 (middle)	25	−95.568	+2.85 m	2.96 m
never crest (downstream)	37	−95.440	+7.06 m	7.06 m

Table 8: The crest-timing groups are spatial bands, and the model-high bias grows monotonically downstream toward the reach the model cannot drain. The upstream band is the calibration target; the middle band is contaminated by the same defect at intermediate strength and cannot serve as held-out data.

model-high signature. Two consequences follow. First, a calibration window has to be placed on the upstream band, where the model-high bias is 0.30 m rather than metres. Crests there fall in event hours 29–41, and the 46 marks in that band are the target of every production number below. Second, the intermediate band is *not* clean held-out data, which rules out the obvious validation design. The out-of-sample test this paper reports is against a second observable (Section 6.5), and cross-validation within the upstream band is the remaining in-observable option.

6.2 How much of the error can roughness explain?

Before asking an optimizer to fit fifteen land-cover classes it is worth asking what any roughness field could achieve, and that question has an optimizer-independent answer. Scaling the entire NLCD field by a single factor α traverses the natural first direction of the problem, which Section 6.4 shows is not its most informative one. Evaluating the peak-WSE misfit along it measures what this paper calls the *authority* of a parameter over an observable: the amount of the model–survey error that changing the parameter can remove, measured without reference to how, or whether, a calibration converges. The largest such amount over the parameter's defensible range, meaning the range inside the stated prior, is the parameter's *ceiling*. Both are lengths, in metres, and fractions of the uncalibrated error, and the paper uses the three words in those senses only.

We ran that scan on the production configuration of Table 3: the 12-hour window over the upstream crest cluster, event hours 29–41, scored against the 46 surveyed marks whose modelled crest falls inside it. Each point is one forward with no adjoint (Table 9).

The window is set by the observable. A high-water mark records an event maximum, so it carries information about roughness only if its crest occurs inside the calibration window; before its crest it is an inequality, and after it a constant. The measured crest times set the window rather than any budget: the 71 marks that crest fall in two groups, 46 in event hours 29–41 and 25 after hour 48 with none between (Table 8), so a window spanning both would spend most of its length integrating marks that had already peaked. The upstream cluster is also the population the model can legitimately be scored against at all, since the downstream marks sit in a reach it cannot drain

α	n range	J	MAE	dry
0.20	0.005–0.032	implicit solve diverges		
0.30	0.008–0.048	6.737×10^2	0.6392	1/46
0.45	0.012–0.072	7.038×10^2	0.6614	1/46
0.60	0.016–0.096	7.406×10^2	0.6776	1/46
0.70	0.019–0.112	7.655×10^2	0.6894	1/46
0.80	0.022–0.128	7.813×10^2	0.6991	0/46
1.00 (NLCD)	0.027–0.160	8.083×10^2	0.7188	0/46

Table 9: Uniform roughness scan on the production configuration (12-hour window, the 46 upstream-band marks); every cell carries $n = \alpha\, n_{\mathrm{NLCD}}$, so the n range column is the whole lookup table scaled by α. J falls monotonically toward lower roughness with no interior minimum: the entire uniform scale is worth 0.08 m against a 0.72 m error, and only at roughness 30% of published values, where n reaches 0.008 and smooth concrete is ≈ 0.012. Within the prior it is worth about 3 cm ($\alpha = 0.70$, itself the optimum implied by the prior width of Section 2.3). The limit at $\alpha = 0.2$ is numerical, not drying; one mark is dry at every point below $\alpha = 0.8$ and none above.

Field	J	ΔJ	MAE	ΔMAE
NLCD prior	808.3	—	0.7188	—
developed classes 21–24 only (71.6% of cells)	786.8	−21.5	0.7306	+0.0118
everything else (28.4%)	827.5	+19.2	0.7268	+0.0080
both (= uniform $\alpha = 0.45$)	703.8	−104.5	0.6614	−0.0574

Table 10: Each half of the domain scaled alone raises the MAE; scaled together they lower it by 0.057 m. In objective units the developed half alone gains 21.5 of the 104.5 the two gain together and the other half alone loses 19.2. Peaks are set by path-integrated conveyance along flow paths that cross both groups, so only domain-coherent changes drain them.

(Section 6.1), a defect no window length repairs. The 46 marks used throughout this paper are therefore those for which the observable means what it is meant to mean. Every number reported here (the uncalibrated baseline, the scans, the calibration, and the spectrum of Section 6.4) is measured on that same window, so they compose.

The entire uniform scale is worth 0.08 m against a 0.72 m error (Figure 2), about 11%, and it reaches that only at $\alpha = 0.3$, Manning values 30% of the published NLCD lookup, as low as $n = 0.008$ where smooth concrete is ≈ 0.012. Inside the prior ($\alpha \gtrsim 0.7$) the scale is worth about three centimetres. The curve is concave with no interior minimum: J falls monotonically toward lower roughness until the implicit solve fails.

An independent measurement gives the same scale. The identifiability twin of Section 5.1 measured the peak-WSE signal induced by a large class perturbation at ~ 0.1 m, the same authority from a different experiment. So about 85% or more of the model-versus-survey residual lies outside the friction term.

The observable constrains one mode, not fifteen. A natural objection is that spatial redistribution should beat uniform scaling, since fifteen classes have freedom a single α does not. We tested it directly by scaling only part of the domain to $\alpha = 0.45$ and leaving the rest at the NLCD prior (Table 10).

By MAE each half alone makes the fit *worse* and the two together remove 0.057 m; by objective the developed half alone gains 21.5 of the 104.5 units the two gain together. Either way the whole

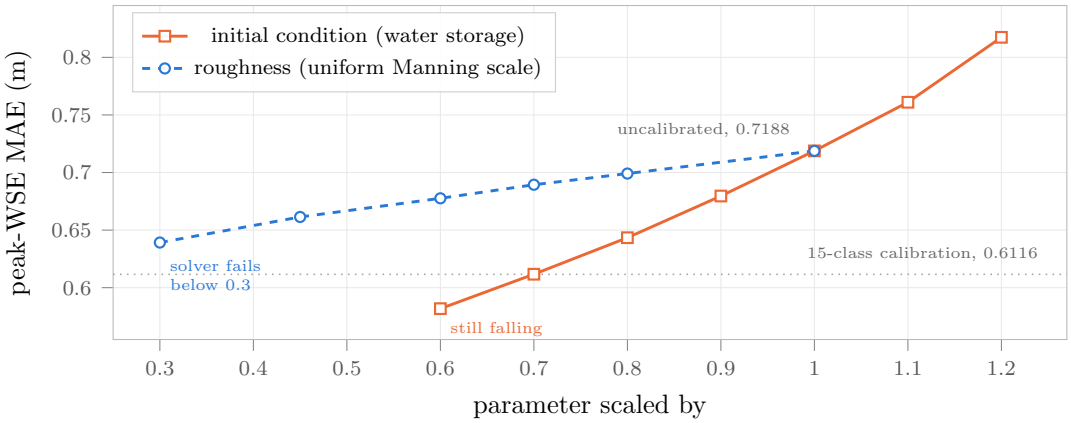


Figure 2: What each parameter can do to the peak-WSE error, on identical axes: the horizontal axis scales the parameter, the vertical axis is the same mean absolute error over the same 46 marks, and both curves pass through the uncalibrated model at 1.0. Roughness is concave and saturates, and its useful end scales the whole table to 0.3, reaching $n = 0.008$ before the implicit solve fails. The initial condition is about four times steeper per unit fractional change, convex, and has not turned over at a 40% reduction in antecedent water. The dotted line is the fifteen-class calibration, which lies off both curves because it redistributes roughness rather than scaling it.

exceeds the sum of its parts. The mechanism is consistent with every other measurement. A mark's peak is set by the *path-integrated* conveyance from upstream to that mark, and those paths cross both groups. Speeding part of a path does not drain it; the resulting fast/slow junction ponds water, so partial changes *raise* peaks. Only a domain-coherent change lowers them.

The conclusion is a design finding, not a tuning observation. What the peak-WSE observable at these marks constrains is the domain-scale, path-integrated conveyance, worth 0.08 m of the 0.72 m discrepancy along the uniform scale and 0.107 m once the classes move as the marks weight them (Section 6.3), and not fifteen classes' worth of information. Section 6.4 counts the combinations on which the marks outweigh the prior: one at the absolute width of the fifteen-class calibration below and about three at ±30%. That count unifies the earlier evidence rather than sitting beside it: the perfect-data twin recovers only the classes that move the domain mean, and the noisy twin pins the others to bounds because they carry no signal to fit, so the optimizer fits noise in those directions instead.

Relation to equifinality. None of this is a new phenomenon: that many different parameter sets reproduce a hydrological observation about equally well is Beven's equifinality thesis [26, 27], and the usual response is to characterize the acceptable set by sampling it. What an adjoint changes is the cost of the diagnosis. Where generalized likelihood uncertainty estimation (GLUE) and its relatives *sample* the equifinal set with many forward runs, the measurements above *measure* its dominant direction directly: the six forward runs of Table 9 put the authority of the whole roughness field at its scale, and the two of Table 10 show that the modes are not separable. The result is the same kind of statement, obtained at a cost that does not grow with the number of parameters, which is what makes it affordable before a calibration rather than after one.

Why this generalizes. The measurement uses nothing specific to roughness. Given a parameter, an observable, and a model error to explain, three steps give the scale of what calibrating that

Manning field	MAE	Δ	where the field sits against the table
NLCD lookup (uncalibrated)	0.7188	—	the table itself
uniform $\alpha = 0.70$	0.6894	-0.029	every class at 0.70 of table
uniform $\alpha = 0.30$	0.6392	-0.080	every class at 0.30; n down to 0.008
calibrated, 15 classes, $\sigma_n = 0.015$	0.6116	-0.107	developed-medium on the floor, 0.036
calibrated, 15 classes, $\sigma_\alpha = 0.30$	0.6154	-0.103	developed-medium 0.036, shrub 0.035
calibrated, 3 classes, $\sigma_n = 0.015$	0.6274	-0.091	developed-medium 0.036, woody wetland 0.029
calibrated, 3 classes, $\sigma_\alpha = 0.30$	0.6290	-0.090	the same two; developed-low 0.21 (2.3×)
calibrated, 3 classes, $\sigma_\alpha = 0.50$	0.6295	-0.089	the same two; developed-low 0.27 (3×)

Table 11: Peak-WSE MAE against the 46 upstream-band marks, every row an achieved in-sample fit. Both fifteen-class calibrations beat the entire uniform scale, including its low end, and beat the best uniform field the prior admits ($\alpha = 0.70$) by 0.078 m: spatial redistribution is worth about three and a half times what a single global scale reaches. The $\sigma_n = 0.015$ field is nine quasi-Newton iterations with the objective flat; the $\sigma_\alpha = 0.30$ field is three, stopped by the wall clock with the objective still falling, and had reached the same misfit ($J_{\text{mis}} = 615.4$) by then. The last column is a fact, not a judgment: the lookup's own entries run from 0.027 (barren) to 0.160 (developed high), its lowest developed entry is 0.040 for developed open land, and $n = 0.036$ and 0.029 on developed-medium and woody wetland therefore sit below anything the table assigns to developed or wetland ground. Whether such values are admissible is a question for the land-cover literature, not for the optimizer. The three-class rows are the calibration Section 6.4 selects.

parameter can accomplish, before any optimizer is written: scan the natural parameter direction, check whether sub-domain changes are separable, and compare the resulting authority against the residual. The scan is an estimate and not a bound: here the calibration of Section 6.3 removes 0.107 m where the scan reaches 0.080, because the direction it varies is not the most informative one (Section 6.4). We suggest the measurement as a routine precondition for calibration studies, which commonly report the misfit reduction achieved without establishing the scale of what was reachable.

6.3 The calibration against the real survey

The scan gives the scale of what a roughness field can do. The question this subsection answers is what a calibration actually achieves against that figure, and at what cost in roughness values. We run the class calibration of Section 2.3 on the same configuration, fifteen NLCD classes in relative variables from the NLCD lookup, at both prior widths, and score every resulting field on the same 46 marks (Table 11).

Calibrated as well as we can currently calibrate it, roughness accounts for 15% **of the** 0.72 **m model–survey error on these marks.** That is the paper's central number and it is an in-sample fit: the 46 marks that define the objective are the 46 the field is scored on. The remaining 85% lies in the rainfall forcing, the antecedent state, the mesh elevation, the datum, or representation error at 30 m, and Section 7 shows one of those, the antecedent state, to be both measurable by the same method and larger.

The 15% is worth having, and the comparison that shows the extra parameters earn their keep is against $\alpha = 0.70$ rather than $\alpha = 0.30$. The latter is the lowest point of the scan the solver reaches and has $n = 0.008$, below any entry in the lookup; the former is the optimum implied by the same prior the calibration uses, and so is the one-parameter competitor that prior allows. Against it the calibration wins by 0.078 m, so the extra parameters are not decoration: *letting roughness vary*

by class removes error that no global scaling can, which is more than the scan alone justifies and the opposite of what the half-domain experiment (Table 10) would have predicted. The reason is measured in Section 6.4, and it is not that fifteen parameters beat one.

Three things qualify the number. First, the objective and the MAE do not move together. The calibrated field's misfit is $J = 615.4$; sliding along the uniform scan's measured MAE-versus-J relation to that same objective gives $\approx 0.596\,\mathrm{m}$ where the calibrated field scores 0.6116, so redistribution buys objective less MAE-efficiently than scaling does and the two should not be quoted interchangeably. That comparison is a counterfactual, and in the calibration's favour: $J = 615.4$ lies below 673.7, the lowest objective the uniform scale reaches before the implicit solve fails, so the uniform field it compares against cannot be run at all.

Second, the run is nine quasi-Newton iterations from the NLCD lookup and was stopped by the 12-hour wall rather than by a tolerance. J fell 18.7% overall but 0.01% on the last iteration while the gradient norm fell 8.5×, which is convergence behaviour without being a converged run.

Third, and this is what the rest of the section is about, the field that achieves the 15% is not one the land-cover table contains. Developed-medium sits on its lower bound throughout, at $n = 0.036$ against the table's 0.040 for developed open land. Widening the prior does not relieve that. Under the fractional prior at the width we assign to the lookup, $\sigma_\alpha = 0.30$, the first quasi-Newton step drove seven of the fifteen classes to a bound, and the run had developed-medium still on the floor and shrub joining it at 0.035 when its budget ran out after three iterations, with the objective still falling (Table 11). A wider prior had reached the same misfit by then, by the same route, and the route is the problem: at that width this observable cannot deliver a fifteen-class roughness field inside the prior.

Projected on the Gauss–Newton eigenvectors of the same prior, the calibrated field lies 9.2 prior standard deviations from the lookup with only 2.9% of that displacement along the one direction on which the marks outweigh that prior (Section 6.4). A fit that improves the score is not thereby the true field: many roughness fields reproduce these peaks about equally well, and this one is chosen by an objective that also absorbs whatever else is wrong with the model. Sections 6.4 and 6.5 put numbers on both halves of that statement, first by counting the combinations on which the marks outweigh the prior and then by testing the result against a second observable.

6.4 How many parameters does the observable support?

Everything above infers the answer from scans. The eigenvalues of the prior-preconditioned Hessian give it directly. The Hessian of a least-squares misfit measures how sharply the observations pin each combination of parameters; the prior, a Gaussian of covariance Γ, measures how sharply the lookup pins them. In coordinates scaled so that the prior has unit variance in every class, the posterior precision, the inverse covariance the parameters would have after assimilating the marks under the linear model, is $I + \Gamma^{1/2} G\, \Gamma^{1/2}$, with G the misfit Hessian. Each eigenvalue λ_i of the whitened misfit Hessian $\Gamma^{1/2} G\, \Gamma^{1/2}$ therefore compares data information against prior information in one direction: the count with $\lambda_i > 1$ is the number of parameters the observable supports, and the eigenvectors say which *combinations* of classes those are, which no scan can. Two limits of the statement should be stated before the numbers. It is a linearization at the lookup, and it describes the information the marks carry there, not the path a calibration takes; the calibrations below move classes as far as both bounds, $\alpha = 0.3$ and 3, and along the one step we measured against its linear prediction (Section 6.5) the mark objective moved 51% of the predicted amount. And it depends on the prior width, so a count is meaningful only with its width attached.

Assembling it. With fifteen classes this needs no low-rank machinery, but it does need the right matrix. Differencing the *gradient* field fails here, and instructively: over a window of this length the objective is dense with wet/dry branch surfaces (Section 2.2.2), and while the adjoint is exact on its own branch the gradient jumps between branches, so a difference quotient samples a discontinuity. Our first attempt returned a matrix with 45% relative asymmetry and eigenvalues to -6.8, which its own consistency check rejected. We therefore assemble the *Gauss–Newton* Hessian, the approximation to the misfit Hessian that keeps the first derivatives of the observations and drops the residual-weighted second derivatives, exact for a linear observation and needing no gradient at all, from observation sensitivities,

$$G = \sigma^{-2}\, S^{\top} W S, \qquad S_{ij} = \partial\big(\max_{t} Hu(t)\big)_i / \partial\alpha_j, \tag{7}$$

with H the observation operator of Section 2.2.2 and W the diagonal 0/1 mark weight, which differences the mark peaks rather than the gradient: one forward per class at α_j raised by 5%. It costs 16 forwards rather than 16 forward-plus-adjoints, and it is positive semi-definite by construction, so the failure mode that invalidated the first attempt cannot recur silently. It also admits a check the first attempt did not: $S^{\top}Wr/\sigma^2$ at the lookup is the misfit gradient, and against the adjoint gradient of the same objective it agrees to within 4% on the three leading classes (-28.4 against -29.5 on developed-low, $+89.7$ against $+90.7$ on developed-medium, $+65.1$ against $+66.2$ on woody wetland, in α) and to within 3 units on every class; the relative misses reach 38% on classes whose gradient is under 6 units. That is one check at one step size. The columns are one-sided 5% secants, finite differences of each peak between the lookup and a 5% rougher class, and have not been shown to converge under step refinement, which a derivative used for inference should be; the same construction on the gauge observable failed exactly that test, which is why no gauge spectrum appears in this paper.

The construction's own assumption, that a mark's peak *time* is locally constant so that the peak *value* is smooth in α, needs the same scrutiny, and on the production window it is not satisfied cleanly: 156 of 690 mark–column pairs (22.6%) move their peak time, against 27 (3.9%) on a two-event-hour pilot of the same configuration. The longer window is the reason. It admits more of each hydrograph, so a crest that was a monotone rising limb over two hours becomes a genuine, and therefore flat, maximum over twelve.

That flatness is what makes the movement harmless, and we checked rather than assumed it. Of the 156, 112 (72%) shift by a single 300-step observation sample, and the resulting change in the peak *value* has median 2.3 mm against a typical peak of 1.5 m: two parts in a thousand, the second-order $O(\Delta t^2 h'')$ cost of stepping one sample off a flat crest. Only ten pairs (1.4%) relocate by more than half an hour, which is a different crest on a bimodal hydrograph. The distinction from the gradient-differencing attempt above is exact rather than rhetorical: there the differenced quantity *jumps* across a branch, whereas $\max_t h$ is *continuous* in α even where its argmax moves, since the two competing maxima are equal at the crossover. A secant of a continuous, piecewise-smooth function remains a valid finite difference; a secant across a discontinuity does not.

The count depends on the prior width. At the absolute prior of the fifteen-class calibration in Table 11, $\sigma_n = 0.015$, the spectrum is $\lambda = 2.78,\ 0.68,\ 0.61,\ 0.32,\ 0.23,\ 0.10, \ldots$ (Figure 3): a single eigenvalue above unity, a spectral gap (the ratio of the first two eigenvalues) of 4.1, and 2.20 degrees of freedom for signal in Rodgers' sense, the sum of $\lambda_i/(1+\lambda_i)$ over all directions, which counts a partly determined direction as a fraction. At the fractional width this paper assigns to the lookup, $\sigma_\alpha = 0.30$, the same sensitivities give $\lambda = 12.7,\ 2.99,\ 1.13,\ 0.85,\ 0.25, \ldots$: three combinations above unity, 3.4 degrees of freedom, and the same three classes leading. Between

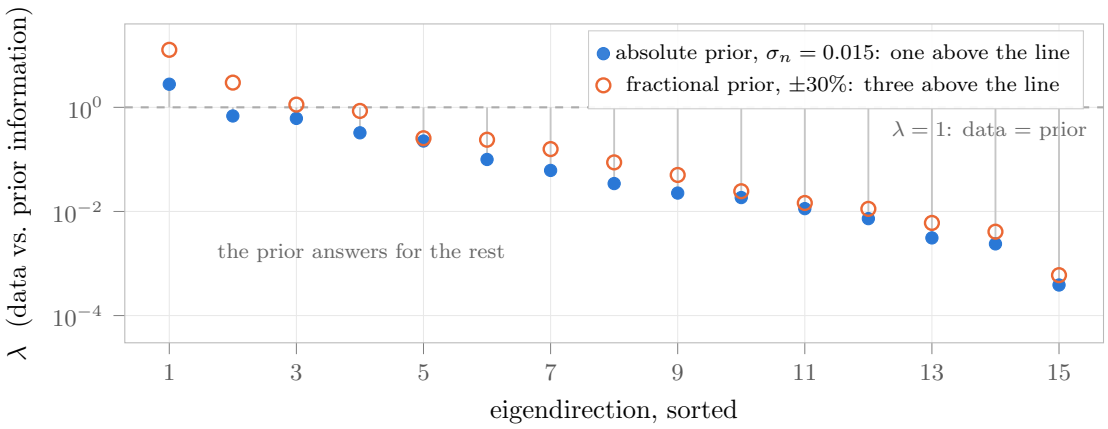


Figure 3: Eigenvalues of the prior-preconditioned Gauss–Newton Hessian over the fifteen land-cover classes, sorted, at the two prior widths the paper uses: the absolute $\sigma_n = 0.015$ of the fifteen-class calibration (filled) and the fractional ±30% assigned to the lookup (open). Above $\lambda = 1$ the marks constrain a direction more than the prior does; below it the prior sets the answer. One direction clears the line at the absolute prior and three at ±30%; the rest fall away over three decades. The figure describes the linearization at the lookup, not the path a calibration takes. The log axis is not cosmetic: on a linear one the cliff would be invisible.

them the count runs one, one, two, three, four at widths of 10, 15, 20, 30 and 50%. So the marks support one roughness combination at the absolute prior and about three at ±30%; in both cases the data outweighs the prior on a few combinations of the fifteen class values and on no others. These counts are properties of the linearization at the lookup.

A shorter pilot of the same configuration (two event hours) gives the same count with a larger leading eigenvalue, 3.03 against 2.78, because over two hours many marks have not crested and a rising limb responds to roughness more sharply than a crest does. The longer window measures the observable the calibration uses and is marginally less informative, not more; identifiability has to come from more marks crossing into the window, not from more trajectory per mark.

The scans and the spectrum agree, and they are independent: no optimizer, no line search, and no calibration enters Eq. (7).

The scan varied nearly the wrong direction. The leading mode, with components −0.64 on developed-medium, +0.59 on woody wetland, −0.36 on developed-low and −0.23 on pasture, is dominated by the large-area classes. Its overlap with the uniform direction the α-scan varies (equal weight per *class*) is 0.218, which for fifteen classes is indistinguishable from random (0.258). Its overlap with the same physical change weighted per *cell* is 0.699. So the informative mode is the domain-scale conveyance mode we claimed, but area-weighted; the α-scan probes it only obliquely. That is why the class calibration beats uniform scaling by 0.078 m (Table 11): it is not that fifteen parameters beat one, it is that the scan's one parameter was the wrong one.

What the calibration actually did. Projecting the calibrated displacement of the absolute-prior fifteen-class field onto the eigenbasis of the same prior separates what the optimizer passed through from what it kept. The calibrated field sits **9.2 prior standard deviations** from the NLCD lookup. Of that motion only 2.9% lies along the leading eigenvector, the single direction on which the marks outweigh this prior; 85.6% lies in directions where data and prior are comparable (λ

NLCD	class	absolute prior	±30% prior
23	developed medium	30%	58%
90	woody wetland	28%	49%
22	developed low	17%	33%
24	developed high	4%	25%
81	pasture	20%	12%
95	emergent wetland	5%	8%
21	developed open	11%	7%
52, 42, 43		$\leq 1\%$	3–5%
11, 31, 41, 71, 82		$\leq 2\%$	$\leq 1\%$

Table 12: What the 46 marks would narrow in each land-cover class: the fractional reduction from prior to posterior standard deviation from the Gauss–Newton Hessian linearized at the lookup, at the absolute prior $\sigma_n = 0.015$ and at the ±30% fractional prior. Ten classes narrow by 5% or less under the absolute prior and eight under the fractional one: any value a calibration reports for them is set by the prior or by the bounds of the search, not by the data.

between 0.2 and 0.7) and 11.5% where the prior alone determines the answer. Per class (Table 12), in the linearization, the marks narrow the prior by 30% on developed-medium and 28% on woody wetland at the absolute prior (58% and 49% at ±30%), by 11–20% on three more, and by 5% or less on the remaining ten.

What the optimizer passed through is the null space. Two iterations in, it had moved deciduous forest to $\alpha = 0.739$, mixed forest to 1.096 and cropland to 1.274, three classes on which the marks would narrow the prior by 2% or less (Table 12), and by iteration nine accumulated curvature had returned all three to within 10% of the prior (0.983, 1.006, 1.098). Those excursions were transients of an under-informed quasi-Newton approximation rather than features of the minimizer: the misfit gradient in uninformative directions is not zero, merely uninformative, and given enough iterations the prior term dominates. A calibration stopped early would have reported them as results, which is an argument for running these problems to convergence even when the objective has visibly flattened.

What it kept is concentrated in the two *best*-informed classes, both pressed against the edge of what the prior permits: developed-medium sits at its $\alpha = 0.3$ lower bound for all nine iterations, and woody wetland is driven to $\alpha = 0.355$, some 4.2σ from its lookup value. Lowering both together is not the leading eigenvector, which pairs them with opposite signs (-0.64 and $+0.59$), but the second, which pairs them with the same sign ($+0.64$ and $+0.61$): over half of the squared displacement lies along that one direction. The absolute prior rates it at $\lambda = 0.68$, data and prior comparable with the prior slightly ahead, so under that prior the calibration moved nine standard deviations in a direction the prior should have held, which is the equifinality Section 6.3 names. The ±30% prior rates the same direction at $\lambda = 2.99$, the second of its three data-determined combinations; re-whitened at that width the field sits 5.7σ from the lookup with 46% of the squared displacement in the three data-determined directions, 39% along this one. So at the width we assign to the lookup the displacement is, in its largest part, in a direction the marks determine, toward roughness below what the published table allows. Whether that value is admissible is not something the optimizer can settle. We put the lookup's uncertainty at 30% or more. That width admits the value for the classes the marks constrain, and it leaves the twelve combinations they do not constrain with nothing to hold them but the bounds of the search, which is where the first step of the wider calibration put seven of the fifteen classes (Section 6.3).

classes	prior	its	J_{mis}	J_{prior}	α_{22}	α_{23}	α_{90}	MAE
—	NLCD lookup	0	808.3	0	1	1	1	0.7188
15	$\sigma_n = 0.015$	9	615.4	41.9	1.627	0.300	0.355	0.6116
3	$\sigma_n = 0.015$	4	648.9	33.2	1.626	0.300	0.301	0.6274
15	$\sigma_\alpha = 0.30$	3	615.4	16.5	1.99	0.300	0.64	0.6154
3	$\sigma_\alpha = 0.30$	3	633.9	15.4	2.34	0.300	0.300	0.6290
3	$\sigma_\alpha = 0.50$	1	627.0	10.0	3.00	0.300	0.300	0.6295

Table 13: Three spectrum-chosen classes against fifteen, calibrated from the NLCD lookup on the production window. "its" is quasi-Newton iterations: the σ_n fifteen-class run and the three-class $\pm 30\%$ run were stopped by the wall clock with the objective flat; the fifteen-class $\pm 30\%$ run was stopped after three iterations with the objective still falling 1.7% per iteration; and the $\pm 50\%$ run stopped in one iteration at a corner of the box, where the projected gradient is zero. J_{mis} and J_{prior} in objective units; $\alpha = n/n_{\text{lookup}}$ for the three active classes, 0.300 being the lower bound; MAE in metres over the 46 marks. Every entry is an achieved in-sample fit.

A direct test: calibrate three classes instead of fifteen. Everything above is a statement about a matrix. It makes a prediction an optimizer can falsify: if the marks inform a few directions, then calibrating only the classes that carry the leading one should recover most of what all fifteen achieved, and if it does not, the information lives outside the leading eigenspace. We ran it (Table 13): the three classes with the largest components in the leading eigenvector (developed-medium, woody wetland, developed-low), the other twelve frozen at the prior and verified to sit there bit-exactly in the output.

Under the absolute prior, three parameters remove 126 of the 151 objective units fifteen remove, 84% of the objective reduction from 20% of the parameters, in four iterations against nine. The prediction survives the change of metric, which is the sharper test: scored on peak-WSE MAE, which they were not fit to, the three reach 0.6274 m, 85% of the 0.107 m that fifteen achieve. The two shares agree here and did not for the fifteen-class field (Section 6.3): a fit confined to the directions the data constrains buys MAE at the same rate it buys objective. The remaining 16% decomposes exactly, the fifteen-parameter field paying 8.8 more units of prior to buy 33.5 more of misfit, so the twelve non-leading classes are not literally decoration but are not where the information is. And the three land where the fifteen put them: developed-low and developed-medium reproduce their fifteen-class values to three digits from a different starting point and active set, so those values come from the marks and not from the start point. Woody wetland is the exception: alone it dives to the floor where the full calibration left it at 0.355, because with its partners frozen it must supply their share of a change the marks constrain only in combination, the equifinality the eigenvector predicts.

The same three classes under the fractional prior. Repeating the run at $\sigma_\alpha = 0.30$, the width we assign to the lookup, and at 0.50 as a bracket above it, gives 0.6290 and 0.6295 m (Table 13): 84% and 83% of the 0.107 m fifteen-class reduction, shares quoted throughout against the best fifteen-class field we obtained. The optimizer's path is short. At $\pm 30\%$ the first step puts all three classes on a bound, as it put seven of fifteen there (Section 6.3), and two more iterations bring developed-low back from $\alpha = 3$ to 2.34; at $\pm 50\%$ the first step lands on a corner of the box, where the projected gradient is zero, and the run stops in one iteration. The Gaussian prior is not what stops it: it contributes 15 units to J at $\pm 30\%$ and 10 at $\pm 50\%$ against a misfit near 630, so the bounds $\alpha \in [0.3, 3]$ do the constraining.

Marks	Supported	That data set is
46	1	the upstream-band marks (this study)
71	2	all admissible marks, 24-hour window
108	3	every QC-passed mark, 72-hour window
324	5	every Harvey mark in-domain, *before* QC
1.2×10^5	15	—

Table 14: How the supported-parameter count scales with survey size at fixed quality ($\sigma = 0.15\,\mathrm{m}$) and at the absolute prior $\sigma_n = 0.015$; a parameter is *supported* when the data narrows it more than the prior does ($\lambda > 1$). At the ±30% width the 46-mark row is already three. At fixed size, improving quality to $\sigma = 0.10\,\mathrm{m}$ buys two more parameters (three in all) and $\sigma = 0.05\,\mathrm{m}$, better than any high-water-mark survey achieves, buys five. The table is a linearized benchmark, not a forecast of what a calibration would do: it assumes independent, equal-variance residual errors and holds the measured per-mark sensitivity, the prior, and the linearization at the lookup fixed, so the longer-window rows describe mark populations only, and a survey with correlated errors would enter through $\Gamma^{1/2} S^\top C^{-1} S\, \Gamma^{1/2}$ rather than through a count.

Three things follow. Developed-medium reaches $\alpha = 0.3$ under every prior and every active set we have run, and woody wetland does whenever its two partners are frozen (0.355 and 0.64 when they are not, the equifinality above), so in the three-class problem those values are set by the data, and they are $n = 0.036$ and 0.029, below the lookup's 0.040 for developed open land. Developed-low's value is set by the prior: it moves from 1.63× to 2.34× to 3× its lookup as the width opens while the MAE moves 0.002 m, which is the flat direction the eigenvector predicted. The three-parameter field therefore lies outside the prior as well. The spectrum selects the three classes, and the calibration of those three reaches a roughness below the lookup's range at every width we assign to it, which is evidence that the calibrated friction is compensating for an error that lives elsewhere (Section 7).

Scaling with survey size. The natural objection is that 46 observations are too few for 15 parameters, and Eq. (7) answers it for the linearization, because λ scales linearly in the number of comparable observations and as σ^{-2} in their quality (Table 14, at the absolute prior). The answer is that more marks help, slowly, and that the supply is exhausted long before the parameterization is justified. Going from the 46 marks of this window to *all* 71 the model can legitimately be scored against would support two parameters. Every QC-passed mark in the domain, over a window long enough to catch all of them, would support three. Reaching five would take every Harvey mark that falls in the domain including the 62% that failed QC because they are channel surveys a 30 m cell cannot represent. Fifteen would take of order 10^5 marks.

The conclusion is therefore not that Manning roughness is unidentifiable. It is that *surveyed peak water-surface elevations at survey accuracy carry between one and three combinations' worth of information about distributed roughness in this basin*, depending on how far the lookup is trusted; that this can be computed from sixteen forward runs at the lookup before any optimizer is written; and that the limitation is a property of the observing system rather than of the method. A study that reported only its misfit reduction would have concluded the opposite.

6.5 Validation against a second observable

The three-class field of Section 6.4 is an in-sample fit: the 46 marks that define its objective are the marks it is scored on. The stream gauges of Table 6 are the only second observable in the basin.

Manning field	22	23	90	gauge J	gauge RMSE	mark MAE
NLCD lookup	0.090	0.120	0.098	31,313	3.24	0.7188
calibrated on the gauges	0.27	0.36	0.171	24,007	2.84	0.7609
calibrated on the marks	0.210	0.036	0.029	30,333	3.19	0.6290

Table 15: The same three classes (developed-low 22, developed-medium 23, woody wetland 90) calibrated against each observable and scored on both, at $\sigma_\alpha = 0.30$ with the other twelve classes frozen at the lookup. Manning n in $\mathrm{s\,m^{-1/3}}$; gauge J is the total objective over 134 above-bed stage records at $\sigma = 0.15$ m treated as independent, including the prior term (47.5 units in the gauge row, 15.4 in the mark row); RMSE $= \sigma\sqrt{2J_{\mathrm{mis}}/134}$ in metres; mark MAE in metres over the 46 upstream-band marks. The gauge calibration is one accepted quasi-Newton iteration stopped by the wall clock; 0.27 and 0.36 were projected onto the $\alpha = 3$ bound. Every entry is an achieved fit on the observable it was calibrated to and a score on the other.

Five of them hold water above the cell bed for part of the window (Buffalo Bayou at Katy and at Houston for all 48 records, Langham Creek at Addicks for 20, Fulshear for 14, Bear Creek for 4: 134 records in all). We calibrated the same three classes on those 134 above-bed stage records, with the survey-grade $\sigma = 0.15$ m and the records treated as independent, and scored the result on the 46 marks (Table 15). The run took one accepted quasi-Newton iteration in its five-hour budget and was stopped by the wall clock; two classes were projected onto the upper bound of the box and the third is interior.

The failure is directional. The gauge calibration raises all three classes where the mark calibration lowered two of them to the floor. The direction does not depend on the observation weight. At the lookup the two objectives' gradients on developed-medium have opposite sign ($\partial J/\partial n = -5.3\times10^4$ for the gauges and $+7.6\times10^2$ for the marks, the prior contributing nothing at its own centre), and no rescaling of σ or of the number of independent records changes a sign; the two agree on developed-low, which both raise. The step the gauges chose also worsens the marks at first order: the mark gradient projected on the gauge step predicts +171 objective units, and the measured change was +87, the 51% of linear that Section 6.4 cites. Along its own objective the step reached 35% of its linear prediction (-7354 measured against -21283 predicted). Scored on the marks, the gauge-calibrated field reaches 0.7609 m against the uncalibrated 0.7188: *calibrating on the gauges at this weight makes the model worse at the marks than not calibrating at all.* The mark-calibrated field, scored on the gauges, lowers their RMSE from 3.24 to 3.19 m.

What the gauges measure. The gauge residual at the lookup is not the size of a roughness error. Splitting the misfit at each gauge into its mean over the window and the variation about that mean (Table 16) puts 99.5% of J in the constant per-gauge offset. The model is 4.9 m too high at Buffalo Bayou at Houston, which carries 82% of the misfit, and 1–2 m too high at three of the other four gauges. What remains in hydrograph shape is 0.24 m RMSE against 3.24 m in all. This is a decomposition of the residual, not of the roughness information: roughness does move the level at these gauges, and the one change tested against it, the field of Table 15 at three times the lookup on two developed classes, removed 0.4 m of the 3.24. Whether any roughness field can remove the remaining 2.8 m is not something these runs measure. The Houston gauge sits in the reach that Section 6.1 found the model cannot drain.

A calibration reported against the gauges alone would show the RMSE falling from 3.24 to 2.84 m, and the roughness values that achieve it, 0.27 and 0.36 on developed-low and developed-medium, sit on the ceiling of the search at three times the lookup, above its largest entry (0.160

Gauge	records	mean residual	shape RMSE	share of J
Buffalo Bayou at Houston	48	+4.90 m	0.38 m	82%
Buffalo Bayou nr Katy	48	+1.94 m	0.07 m	13%
Buffalo Bayou nr Fulshear	14	+1.97 m	0.06 m	4%
Langham Ck nr Addicks	20	−0.61 m	0.12 m	0.6%
Bear Ck nr Barker	4	+1.20 m	0.01 m	0.4%

Table 16: The gauge misfit at the NLCD lookup, gauge by gauge, over the 134 above-bed records: model minus observed water-surface elevation averaged over the window, the RMS variation about that mean, and each gauge's share of J. Summed, the offsets carry 99.5% of J and the shape 0.5%: RMSE 3.24 m in all, 0.24 m in shape alone.

for developed high). The reduction is an achieved fit, and values on a bound are the sign, visible without the marks, that the fit has run to the edge of what the search allows. Neither is evidence about friction.

Fit, uncertainty, and skill. Three kinds of number appear in this section and the last, and they are not interchangeable. An *achieved fit* is the misfit of one specific roughness field on the observations its calibration used, from a forward run at that field: every MAE and objective in Tables 11, 13 and 15, and the ceiling of Section 6.2. It says what the model did at that field and nothing about whether the field is right or would transfer. A *linearized uncertainty* comes from the sensitivity matrix at the lookup through the Gauss–Newton Hessian: the eigenvalues and counts, the widths in Table 12, the benchmark of Table 14, and the first-order prediction above of the gauge step's effect on the marks. It says how far the observations could narrow each combination of classes under the linear model at the prior, for a stated prior width, and nothing about the values a calibration reaches or the error it removes. *Held-out skill* is the score of a calibrated field on observations that did not enter its objective, either a second observable or a hold-out within the same one. This paper has only the first kind, the two cross-scores of Table 15: the gauge-calibrated field is worse than the lookup at the marks, and the mark-calibrated field improves the gauges by 0.05 m of 3.24. The three-class field's 0.090 m improvement at the marks is therefore a fit and not a skill, and the three-combination count is an uncertainty at the prior, not a result of the calibration. The two observables agree on one thing: the land-cover table is not where this model's error lives.

7 Where else the error lives: the initial condition

Roughness, calibrated as well as we can calibrate it, explains 15% of this model's error against the marks. Something explains the other 85%, and the candidates (rainfall forcing, mesh elevation, datum, representation error, the state the window starts from, and the water the outlet boundary admitted before the window opened) are not all equally measurable. One of them is not even static during the event: a coupled land–hydrodynamics–sediment simulation of a Houston watershed under Harvey puts event-scale deposition at 8.0 million cubic metres, 2.3 million of it along major channels and floodplains [28], so the bed elevation this model holds fixed is one the flood was itself changing. This section points the ceiling measurement of Section 6.2 at the one candidate it can probe with a single scan direction: the initial condition. The initial state is also the input a variational initialization would control, so the measurement doubles as a feasibility probe for initial-state estimation with the same adjoint machinery, which the conclusions take up.

Our window begins at event hour 29 from a checkpoint of the 72-hour forward, and the natural

IC scale a	J	MAE	ΔMAE per 0.1
0.80	6.652×10^2	0.6434	—
0.90	7.284×10^2	0.6796	+0.0362
1.00 (checkpoint)	8.083×10^2	0.7188	+0.0392
1.10	9.071×10^2	0.7610	+0.0422
1.20	1.025×10^3	0.8174	+0.0564

Table 17: Peak-WSE misfit against antecedent water storage. The response is monotone over the whole range with no interior optimum, straight to about 1% between $a = 0.8$ and 1.1 and convex above it: adding water hurts at an accelerating rate. The model holds systematically too much water at hour 29.

single direction to scan is the amount of water that checkpoint holds. Scaling all three conserved variables by a common factor a changes antecedent storage while leaving every velocity unchanged, since $u = (hu)/h$ is invariant. Each point is one forward (Table 17).

Three things follow, and they matter more than the roughness result.

The initial state has about four times the authority of roughness (Figure 2). Per unit fractional change, d MAE is 0.392 for the initial condition over its well-sampled range ($a \in [0.8, 1.1]$) against 0.098 for a uniform roughness scale over the same width inside the prior ($\alpha \in [0.7, 1]$). Like for like at a 20% perturbation: 0.075 m versus 0.020 m. Whether a 20% error in water stored after a 29-hour spin-up under radar-derived rainfall is plausible is taken up at the end of this section; Manning values at 30% of the published table lie below the table's own value for open land.

The response has the opposite curvature to roughness's. $J(\alpha)$ for roughness is concave and saturating, consistent with a parameter acting indirectly through path-integrated conveyance. $J(a)$ for the initial state is straight to about 1% between $a = 0.8$ and 1.1 and *convex* above, steepening as water is added, and it does not turn over anywhere in the range. Extending the scan below the table confirms it: at $a = 0.6$ (a 40% reduction in antecedent water) the MAE is still falling, to 0.5818 m (Figure 2). Neither the slope nor the sign gives any indication of an optimum near the checkpoint value. That is the signature of a systematic bias rather than a poorly-tuned parameter: the model does not hold the wrong *distribution* of water at hour 29, it holds too much of it.

It is a diagnosis, not a calibration target. We are not proposing to calibrate the initial condition against these marks. Over this window the initial state carries 3 unknowns on each of 2.93M cells against 46 peak observations, and everything Section 6.2 establishes about identifiability applies with almost six orders of magnitude more freedom than the fifteen classes: such a calibration would fit the marks exactly and mean nothing. What the scan does establish is the weaker and more useful claim that the residual these marks measure lives substantially in the water balance (in the rainfall forcing, the antecedent state, or the inflow the outlet boundary admitted) rather than in the friction, which is where a roughness calibration alone would have kept looking.

One caveat bounds all three. The checkpoint is a *model* state, not an observation, so it already contains accumulated forcing and elevation error; the scan perturbs that state rather than an independent measurement of it. A calibration of the initial condition would therefore absorb such error rather than correct it, and could quietly launder the downstream drainage defect of Section 6.1 into a "corrected" initial state, the same trap as scoring against the 37 marks the model cannot drain. Part of a 20% water-balance error at hour 29 is already measured and is not the forcing's: about 19% of the water the domain holds at hour 29 entered through the outlet boundary (Section 6.1), though where it sits at that hour is not measured. Whether the forcing contributes an error of that

size is a question for the forcing data, not for the optimizer, and we have not quantified it: that needs a spin-up of one to two months before the event rather than 29 hours. What can be said is that 20% is an ordinary scale of hydrologic uncertainty at high flow (observed streamflow itself carries uncertainty of that order [29]), and that the uncertainty study of this event in [24] finds precipitation and mesh resolution to dominate the simulated inundation over the choice of outlet boundary condition, which points the same way. The 20% is an illustrative perturbation, not a measured error.

8 Conclusions and outlook

An exact, verified Jacobian turns out to be the single artifact from which everything else follows cheaply: adjoint state and parameter sensitivities, gradient-based calibration, and implicit stepping. The capability is production-ready in the sense that matters for an operational code: behind a flag, FD-gated in CI, and with the verification baseline (FD coloring) kept alive in the configuration system.

The second artifact is a measurement rather than a capability, and it is the one we would most like others to copy. Asking what fraction of a model's error a parameter is *able* to explain is cheap, optimizer-independent, and it reframes what a calibration result means. Here it put roughness at 4% of the error inside the prior and 11% at the scan's low end, below the table; the calibration then reached 15% in sample, beating every global scaling and confirming that letting roughness vary by class removes error a single global factor cannot. What makes the measurement worth copying is not that number but the two it led to. Pointed at the residual instead of the parameter, the same machinery isolated a reach the model cannot drain; pointed at the initial condition, it found more authority than roughness has. A calibration study that had only reported its misfit reduction would have found neither.

Next steps, in order. First, the one out-of-sample test we ran, against the stream gauges, failed in sign as well as in size (Section 6.5); the remaining test of the three-class field is a hold-out within the upstream band, because the middle band carries the drainage defect. Second, the water balance: the initial-condition scan says the antecedent state carries more of this residual than the friction does, which makes the forcing and the initial condition, not the roughness, the next thing to calibrate or diagnose, with the machinery applying unchanged and dJ/du_0 already verified. Third, the boundary: the closed-perimeter idealization the drainage finding implicates, a divide we read the event as having exceeded, and an outlet condition that admitted water for 38 of the 72 hours (Section 6.1). Finally, coupling the gradient path to PyTorch through the existing PETSc–PyTorch bridge for learned-physics and hybrid data-assimilation experiments.

A closing note on cost. Checkpointing makes the long-window adjoint memory-feasible, but at the 30 m mesh's CFL-limited $\Delta t = 0.25$ s a full 36-hour Hurricane Harvey gradient still costs several forward sweeps over half a million steps. The affordable path stacks reductions that are all now in place. First, fully implicit stepping at CFL-free time steps: backward Euler with the assembled Jacobian carries the 30 m, 2.93M-cell Harvey-region mesh at $\Delta t = 1$ s, a step the differentiable explicit path cannot take at any tested size (Section 4), with Newton converging in about two iterations per step behind a block-Jacobi-preconditioned Krylov solve at converged inner tolerances; larger implicit steps are under investigation. Second, GPU execution of the entire gradient pipeline: the right-hand side, the assembled Jacobian and its transpose solves, the preconditioner setup, the parameter Jacobian, the observation operator, and the revolve-checkpointed trajectory are all device-resident. On four A100 GPUs, a forward-plus-adjoint gradient of a one-simulated-hour window on that mesh (3,600 implicit steps, 400 in-memory checkpoints) takes about nine minutes,

and one TAO iteration of a dense-gauge twin calibration (418,076 gauges, 39-step window) takes 1.7 s, about 19× faster than one 64-core CPU socket of the same system. Device and host runs of the same binary and partition produce objectives and gradients identical to every printed digit, so the finite-difference gates of Table 1 carry over unchanged. Third, land-cover-class parameterization (nine or fewer quasi-Newton iterations in Table 13, against the hundreds the per-cell twins of Section 5 needed) and calibration windows placed on the storm peak rather than the full event.

Acknowledgements

We thank Emil Constantinescu for a review that changed how this paper reports its numbers. Three of his points are carried in the text: that a local uncertainty estimate, an achieved fit and held-out predictive skill are three different quantities and each number must say which it is; that the offset and shape decomposition of the gauge misfit is a statement about the residual rather than about which part of it roughness can move; and that a single finite-difference check at one step size does not establish that a sensitivity has converged (Sections 6.4 and 6.5). Section 6.5 gives the part of his question, whether the two observables are complementary, redundant or opposed, that needs no gauge sensitivity matrix: the signs of the two gradients at the lookup. The subspace comparison he asked for waits on a gauge sensitivity that converges under step refinement, which Section 6.4 reports we do not have.

This research was supported by the U.S. Department of Energy (DOE), Office of Science, Office of Biological and Environmental Research and Advanced Scientific Computing Research, Scientific Discovery through Advanced Computing (SciDAC) program.

This material is based upon work supported by the U.S. Department of Energy, Office of Science, Office of Advanced Scientific Computing Research, Scientific Discovery through Advanced Computing (SciDAC) Program through the FASTMath Institute, under contract number DE-AC02-05CH11231 at Lawrence Berkeley National Laboratory.

This research used resources of the National Energy Research Scientific Computing Center, a DOE Office of Science User Facility supported by the Office of Science of the U.S. Department of Energy under Contract No. DE-AC02-05CH11231 using NERSC award ASCR-ERCAP0039362.

Use of AI

Claude (Anthropic) was used throughout the preparation of this work: in developing the capability described here, in writing and running the analysis scripts behind its figures and tables, and in drafting and revising the manuscript. Every number reported comes from the runs recorded in the Artifact Description. The authors verified the results against those run logs and are responsible for the content of this paper.

Code and data availability

RDycore is open source at `https://github.com/RDycore/RDycore`. The analytic Jacobian, Kokkos GPU assembly, implicit-stepping, discrete-adjoint, and calibration capability of this paper is on its `adams/gpu-implicit` branch, at the tag `manning-calibration-arxiv-v1`, behind the `numerics.jacobian` and `adjoint` configuration flags; the verification gates of Table 1 run in its `ctest` suite. The Artifact Description, `papers/manning-calibration/README.md` at that tag, maps each figure and table to the campaign scripts (`plans/campaigns/`) and to the archived output logs and per-mark peak dumps (`logs/`) behind it. Hurricane Harvey high-water marks are the USGS Short-Term Network

survey, retrieved through the STN Flood Event Viewer API (`https://stn.wim.usgs.gov`) with the retrieval script and the filtered mark table in `data/harvey_hwm/`; stage records are from the USGS National Water Information System (NWIS), processed in `data/harvey_gauges/`; land-cover roughness tables and sampling scripts are in `data/nlcd/`; rainfall is the Multi-Radar Multi-Sensor (MRMS) product.

References

[1] Yan Ding, Yafei Jia, and Sam S. Y. Wang. Identification of Manning's roughness coefficients in shallow water flows. *Journal of Hydraulic Engineering*, 130(6):501–510, 2004.

[2] Xianqiang Chen et al. Adjoint model of shallow water equations based on the finite volume method and unstructured meshes. *Abstract and Applied Analysis*, 2014:407468, 2014. Twin-experiment inversion of Manning roughness; velocity vs. stage observation sensitivity.

[3] Asier Lacasta, Mario Morales-Hernández, Pilar García-Navarro, et al. A GPU accelerated adjoint-based optimizer for inverse modeling of the two-dimensional shallow water equations. *Computers & Fluids*, 2016.

[4] Jérôme Monnier et al. DassFlow: Data assimilation for free-surface flows (DassHydro platform). `https://dasshydro.github.io`, 2025. 2D finite-volume shallow water with variational DA; Manning, bathymetry, and discharge inference incl. SWOT/AirSWOT and video-derived surface velocity.

[5] Xijun Lai and Jérôme Monnier. Assimilation of spatially distributed water levels into a shallow-water flood model. Part I: Mathematical method and test case. *Journal of Hydrology*, 377(1–2):1–11, 2009.

[6] Pierre Brisset, Jérôme Monnier, Pierre-André Garambois, and Hélène Roux. River discharge estimation from synthetic SWOT-type observations using variational data assimilation and the full Saint-Venant hydraulic model. *Journal of Hydrology*, 558:176–195, 2018.

[7] Tuomas Kärnä et al. Efficient optimization of a regional water elevation model with an automatically generated adjoint. *Journal of Advances in Modeling Earth Systems*, 15, 2023. Spatially varying Manning friction calibrated for the Baltic Sea with Thetis/Firedrake/pyadjoint.

[8] Simon C. Warder, Kevin J. Horsburgh, and Matthew D. Piggott. Adjoint-based sensitivity analysis for a numerical storm surge model. *Ocean Modelling*, 160:101766, 2021.

[9] Soheil Radfar. How sparse and how noisy? Systematic benchmarking of inverse physics-informed neural networks for Manning friction estimation in shallow water equations. *Physics of Fluids*, 38(8):086611, 2026.

[10] Léo Pujol, Pierre-André Garambois, Carole Delenne, and Jean-Louis Perrin. Adjoint-based sensitivity analysis and assimilation of multi-source data for the inference of spatio-temporal parameters in a 2D urban flood hydraulic model. *Journal of Hydrology*, 2024. DassFlow2D; adjoint by source-to-source AD (Tapenade). Infers distributed friction from multi-source observations including high-water marks, with derivative-based global sensitivity measures used to choose the friction patch spatialization.

[11] Zhi Li. Inunda: A GPU-native, agent-enabled, differentiable solver for high-resolution flood inundation modeling. arXiv:2607.09614, 2026. PyTorch local-inertial solver; roughness/bed/infiltration by gradient descent; Hurricane Harvey hindcast, Harris County TX.

[12] Xiaofeng Liu et al. Scientific machine learning of flow resistance using universal shallow water equations with differentiable programming. *Water Resources Research*, 61, 2025. Hydrograd (Julia/SciML): AD-based Manning inversion and neural flow-resistance terms.

[13] Elsa Cardoso-Bihlo and Alex Bihlo. A solver-in-the-loop framework for end-to-end differentiable coastal hydrodynamics. arXiv:2604.07129, 2026. AegirJAX: differentiable non-hydrostatic shallow-water solver in JAX.

[14] Tadd Bindas et al. Improving river routing using a differentiable Muskingum-Cunge model and physics-informed machine learning. *Water Resources Research*, 60, 2024. Differentiable routing inferring Manning roughness and channel geometry with neural networks.

[15] Shengyu Kang, Jiabo Yin, and Dai Yamazaki. CaMa-Flood-GPU: A GPU-based hydrodynamic model implementation for scalable global simulations. *Geoscientific Model Development*, 19:5623–5640, 2026.

[16] Patrick Heimbach, Chris Hill, and Ralf Giering. An efficient exact adjoint of the parallel MIT general circulation model, generated via automatic differentiation. *Future Generation Computer Systems*, 21(8):1356–1371, 2005.

[17] Gaël Forget, Jean-Michel Campin, Patrick Heimbach, Christopher N. Hill, Rui M. Ponte, and Carl Wunsch. ECCO version 4: an integrated framework for non-linear inverse modeling and global ocean state estimation. *Geoscientific Model Development*, 8(10):3071–3104, 2015.

[18] Matthew J. Hoffman, Mauro Perego, Stephen F. Price, William H. Lipscomb, Tong Zhang, Douglas Jacobsen, Irina Tezaur, Andrew G. Salinger, Raymond Tuminaro, and Luca Bertagna. MPAS-Albany Land Ice (MALI): a variable-resolution ice sheet model for Earth system modeling using Voronoi grids. *Geoscientific Model Development*, 11(9):3747–3780, 2018.

[19] Mauro Perego, Stephen Price, and Georg Stadler. Optimal initial conditions for coupling ice sheet models to Earth system models. *Journal of Geophysical Research: Earth Surface*, 119(9):1894–1917, 2014.

[20] Gautam Bisht, Donghui Xu, Jeffrey Johnson, Jed Brown, Matthew Knepley, Mark Adams, Dongyu Feng, Dalei Hao, Darren Engwirda, Mukesh Kumar, et al. Development of a river dynamical core for E3SM to simulate compound flooding on Exascale-class heterogeneous supercomputers. *Environmental Modelling & Software*, 197:106804, 2025.

[21] Hong Zhang, Emil M. Constantinescu, and Barry F. Smith. PETSc TSAdjoint: A discrete adjoint ODE solver for first-order and second-order sensitivity analysis. *SIAM Journal on Scientific Computing*, 44(1):C1–C24, 2022.

[22] Xilin Xia and Qiuhua Liang. A new efficient implicit scheme for discretising the stiff friction terms in the shallow water equations. *Advances in Water Resources*, 117:87–97, 2018.

[23] Steven J. Benson and Jorge J. Moré. A limited memory variable metric method in subspaces and bound constrained optimization problems. Technical Report ANL/MCS-P909-0901, Argonne National Laboratory, Mathematics and Computer Science Division, 2001.

[24] Donghui Xu, Gautam Bisht, Darren Engwirda, Dongyu Feng, Zeli Tan, and Valeriy Y. Ivanov. Uncertainties in simulating flooding during Hurricane Harvey using 2D shallow water equations. *Water Resources Research*, 61(1):e2024WR038032, 2025.

[25] Harris County Flood Control District and Texas Water Development Board. Final Study Report: Cypress Creek Overflow Management Plan. Technical Report 1248321466, Texas Water Development Board, 2015. `https://www.twdb.texas.gov/publications/reports/contracted_reports/doc/1248321466_HCFCD.pdf`.

[26] Keith Beven and Andrew Binley. The future of distributed models: Model calibration and uncertainty prediction. *Hydrological Processes*, 6(3):279–298, 1992.

[27] Keith Beven. A manifesto for the equifinality thesis. *Journal of Hydrology*, 320(1–2):18–36, 2006.

[28] Dongyu Feng, Zeli Tan, Donghui Xu, Lingcheng Li, and Gautam Bisht. An integrated modeling framework for sediment dynamics during urban flooding: Application to Hurricane Harvey in Houston. *Water Resources Research*, 62(5):e2025WR042040, 2026.

[29] Julie E. Kiang, Chris Gazoorian, Hilary McMillan, Gemma Coxon, Jérôme Le Coz, Ida K. Westerberg, Arnaud Belleville, Damien Sevrez, Anna E. Sikorska, Asgeir Petersen-Øverleir, Trond Reitan, Jim Freer, Benjamin Renard, Valentin Mansanarez, and Robert Mason. A comparison of methods for streamflow uncertainty estimation. *Water Resources Research*, 54(9):7149–7176, 2018.